Systems/Circuits

Hypothalamic Tuberomammillary Nucleus Neurons: Electrophysiological Diversity and Essential Role in Arousal Stability

Akie Fujita,[1,2,3]* Patricia Bonnavion,[4,5]* Miryam H. Wilson,[1] Laura E. Mickelsen,[1,3] Julien Bloit,[6] Luis de Lecea,[4]** and Alexander C. Jackson[1,3]**

Departments of [1]Physiology and Neurobiology and [2]Biomedical Engineering, and [3]Connecticut Institute for the Brain and Cognitive Sciences, University of Connecticut, Storrs, Connecticut 06269, [4]Department of Psychiatry and Behavioral Sciences, Stanford University School of Medicine, Stanford, California 94305, [5]Laboratory of Neurophysiology, Université Libre de Bruxelles (ULB)-UNI, 1050 Brussels, Belgium, and [6]Independent software engineer, 1190 Brussels, Belgium

Histaminergic (HA) neurons, found in the posterior hypothalamic tuberomammillary nucleus (TMN), extend fibers throughout the brain and exert modulatory influence over numerous physiological systems. Multiple lines of evidence suggest that the activity of HA neurons is important in the regulation of vigilance despite the lack of direct, causal evidence demonstrating its requirement for the maintenance of arousal during wakefulness. Given the strong correlation between HA neuron excitability and behavioral arousal, we investigated both the electrophysiological diversity of HA neurons in brain slices and the effect of their acute silencing *in vivo* in male mice. For this purpose, we first validated a transgenic mouse line expressing cre recombinase in histidine decarboxylase-expressing neurons (*Hdc*-Cre) followed by a systematic census of the membrane properties of both HA and non-HA neurons in the ventral TMN (TMNv) region. Through unsupervised hierarchical cluster analysis, we found electrophysiological diversity both between TMNv HA and non-HA neurons, and among HA neurons. To directly determine the impact of acute cessation of HA neuron activity on sleep–wake states in awake and behaving mice, we examined the effects of optogenetic silencing of TMNv HA neurons *in vivo*. We found that acute silencing of HA neurons during wakefulness promotes slow-wave sleep, but not rapid eye movement sleep, during a period of low sleep pressure. Together, these data suggest that the tonic firing of HA neurons is necessary for the maintenance of wakefulness, and their silencing not only impairs arousal but is sufficient to rapidly and selectively induce slow-wave sleep.

Key words: arousal; histamine; membrane properties; optogenetics; slow-wave sleep; tuberomammillary

---

Significance Statement

The function of monoaminergic systems and circuits that regulate sleep and wakefulness is often disrupted as part of the pathophysiology of many neuropsychiatric disorders. One such circuit is the posterior hypothalamic histamine (HA) system, implicated in supporting wakefulness and higher brain function, but has been difficult to selectively manipulate owing to cellular heterogeneity in this region. Here we use a transgenic mouse to interrogate both the characteristic firing properties of HA neurons and their specific role in maintaining wakefulness. Our results demonstrate that the acute, cell type-specific silencing of HA neurons during wakefulness is sufficient to not only impair arousal but to rapidly and selectively induce slow-wave sleep. This work furthers our understanding of HA-mediated mechanisms that regulate behavioral arousal.

Introduction

Dynamic transitions between sleep and arousal states are driven by the ascending arousal system, a component of which is a population of projection neurons that release histamine (HA), a mono-aminergic neurotransmitter synthesized from L-histidine through histidine decarboxylase (HDC; Haas et al., 2008). HA-synthesizing neurons are strongly conserved throughout vertebrate phylogeny from zebrafish to humans, reflecting the important

roles they play in many aspects of physiology and behavior (Schwartz et al., 1991; Lin, 2000; Brown et al., 2001; Haas and Panula, 2003; Saper et al., 2005; Passani et al., 2007; Haas et al., 2008; Saper et al., 2010; Thakkar, 2011; Panula and Nuutinen, 2013; Scammell et al., 2017). In mammals, HDC-expressing, HA-synthesizing neurons are only found in the tuberomammillary nucleus (TMN) of the posterior hypothalamus (Watanabe et al., 1983; Panula et al., 1984; Wouterlood et al., 1986; Ericson et al., 1987). TMN HA neurons extend a widespread, though diffuse, network of unmyelinated fibers throughout the CNS, including interconnections with other arousal-related neuromodulatory systems (Takeda et al., 1984; Takagi et al., 1986; Inagaki et al., 1988; Panula et al., 1989). Disruptions in HA neurotransmission have been implicated in a variety of neuropsychiatric disorders (Panula and Nuutinen, 2013; Baronio et al., 2014; Shan et al., 2015a,b), for which HA receptors are promising therapeutic targets (Lin et al., 2011; Passani and Blandina, 2011; Schwartz, 2011).

Multiple lines of functional evidence suggest that the hypothalamic HA system regulates aspects of arousal and wakefulness. Functional inactivation of the posterior hypothalamus/TMN or pharmacological inhibition of HA signaling produces somnolence in multiple experimental preparations (Naquet et al., 1966; Swett and Hobson, 1968; McGinty, 1969; Lin et al., 1988, 1989, 1994; Nicholson et al., 1991). Furthermore, genetic loss-of-function manipulations have implicated HA transmission in cortical activation and behavioral arousal (Parmentier et al., 2002, 2016; Anaclet et al., 2009). Consistent with the role of HA neurons in behavioral arousal, cFos expression in HA neurons (Ko et al., 2003) and HA release in the anterior hypothalamus (Strecker et al., 2002), cortex (Chu et al., 2004), and basal forebrain (Zant et al., 2012) have been found to be greater during periods of wakefulness. Importantly, the electrical activity of HA neurons in vivo has been shown to be tightly correlated with arousal state. In vivo single-unit electrophysiological recordings demonstrate that putative HA neurons exhibit slow, regular pacemaking activity (<10 Hz; Reiner and McGeer, 1987). This activity displays a distinct wake–active firing pattern; firing most rapidly during attentive waking, more slowly during quiet waking, and silent during all sleep stages (Steininger et al., 1999; Vanni-Mercier et al., 2003; Takahashi et al., 2006; Sakai et al., 2010). The observation that HA neurons cease firing immediately preceding sleep and resume immediately following awakening (Takahashi et al., 2006) suggests a mechanism whereby the silencing of HA neuron activity may be necessary for sleep induction. Lacking, however, is direct, causal evidence that acute silencing of HA neurons either impairs or indeed abolishes wakefulness and promotes sleep.

To further our understanding of the role of HA neurons in sleep–wake states, we undertook an anatomical, electrophysiological, and behavioral analysis of genetically identified HA neurons in adult mice, using a previously uncharacterized Hdc-Cre transgenic line generated by the Gene Expression Nervous System Atlas (GENSAT) Project (Gong et al., 2007). We first evaluated the fidelity with which cre-mediated recombination occurs in Hdc-Cre mice and then performed a comprehensive in vitro

electrophysiological phenotyping of the membrane properties of both genetically identified HA and non-HA neurons within the ventral TMN (TMNv) region, followed by classification using unsupervised hierarchical cluster analysis. Finally, we used an optogenetic approach to silence HA neuron excitability in awake and behaving mice to test the hypothesis that acute suppression of HA neuron activity not only disrupts wakefulness but permits the induction and maintenance of sleep.

Materials and Methods

Animals. All animal use was in accordance with guidelines approved by both the University of Connecticut and Stanford University School of Medicine Institutional Animal Care and Use Committees. All experiments were furthermore conducted according to National Institutes of Health guidelines for the humane care and treatment of laboratory animals. We used the mutant mouse line Tg(Hdc-Cre)[IM1Gsat/Mmucd] (RRID: MMRRC_032079-UCD), referred to here as Hdc-Cre, for all anatomical, in vitro electrophysiological, and in vivo behavioral experiments. Hdc-Cre is a bacterial artificial chromosome (BAC) transgenic cre line, with cre recombinase expression driven by the Hdc promoter, generated as part of the GENSAT Project at Rockefeller University (Gong et al., 2003,; 2007), and acquired through the Mutant Mouse Regional Resource Centers (MMRRCs; RRID:SCR_002953). Hdc-Cre mice were backcrossed to C57BL/6 (stock #000664, The Jackson Laboratory; RRID: IMSR_JAX:000664) over several generations and maintained as heterozygotes. For characterization of cre-mediated recombination in the whole brain, these mice were crossed with a cre-dependent tdTomato (td-Tom) reporter line, B6.Cg-Gt(ROSA)26Sor[tm14(CAG-tdTomato)Hze]/J), also known as Ai14 from the Allen Institute for Brain Science (Madisen et al., 2010) and acquired from The Jackson Laboratory (stock #007908; RRID: IMSR_JAX:007908). For breeding purposes, heterozygote Hdc-Cre animals were bred to homozygote Ai14 mice to generate lines of Hdc-Cre; tdTom mice. For slice electrophysiology, we used male Hdc-Cre;tdTom mice along with male wild-type mice with a C57BL/6 background as controls. Finally, for in vivo behavioral experiments, we used male Hdc-Cre mice for both experimental and control conditions.

Fixation and sectioning. Animals (1–3 months old) were anesthetized with isoflurane and perfused transcardially with 10–15 ml of saline, followed by 35–40 ml of 4% paraformaldehyde (PFA) in PBS for tissue fixation. Animals were then decapitated, and brains were removed and placed in 4% PFA overnight. Brains were then transferred into 30% sucrose for 36–48 h for cryoprotection followed by rapid freezing in cold isopentane and stored at −80°C. Frozen brains were then sectioned in either the coronal (40–50 μm) or parasagittal (50 μm) orientation on a cryostat at −20°C and stored in PBS at 4°C.

Immunohistochemistry. Immunostaining was performed on free-floating brain sections containing the TMN. Sections were washed in PBS followed by PBS plus 0.2% Tween 20 (PBST), blocked in 2% donkey normal serum (DNS) in PBST for 2 h, and incubated on a shaker overnight (~17 h) at room temperature with an anti-HDC primary antibody (Rb anti-HDC; 1:1000; Acris). Sections were then washed in PBST and incubated for 2 h at room temperature in a secondary antibody Dk-anti-Rb Alexa Fluor 488 (1:500; Abcam; RRID:AB_2636877) or Dk-anti-Rb Alexa Fluor 594 (1:500; Abcam; RRID:AB_141637). After secondary antibody staining, sections were then washed in PBST, followed by PBS, and finally mounted onto slides using hard-set Vectashield containing 4′,6′-diamidino-2-phenylindole dihydrochloride (DAPI; Vector Laboratories; RRID:AB_2336788). Parasagittal sections that did not undergo immunohistochemistry were also washed in PBS and mounted using Vectashield.

Fluorescence and confocal microscopy. Slides were imaged using a Zeiss Axio Imager M2 to obtain fluorescence images or Leica TCS SP2 or SP8 laser-scanning confocal microscopes to obtain confocal images. Confocal images were obtained at a magnification of 40×. Fluorescence images of the hypothalamus were collected at a magnification of 10×, and in many cases during collection, 10× images were tiled and stitched to view the whole hypothalamus or the whole slice.

Image analysis. ImageJ (http://imagej.nih.gov/ij/; RRID:SCR_003070) was used to visualize confocal stacks and quantify cell types in each stack. In all experiments, confocal stacks were collected exclusively in the TMNv. For quantification, each identifiable cell was examined for fluorescence and placed into one of three defined categories using the Cell Counter plugin for ImageJ (Kurt De Vos, University of Sheffield, Sheffield, UK; http://rsbweb.nih.gov/ij/plugins/cell-counter.html). In experiments using *Hdc*-Cre;tdTom brains (*n* = 3 mice) counterstained for HDC-immunoreactive (IR) using Alexa Fluor 488, cells were counted as follows: (1) tdTom⁺, (2) HDC-IR, or (3) tdTom⁺/HDC-IR. These data were then totaled across all sections analyzed in the experiment and used to calculate the quantification measures. For quantification, we calculated the percentage of tdTom-expressing cells that were HDC-IR (specificity), and the percentage of HDC-IR cells that were tdTom expressing (penetrance) in the TMNv.

Slice preparation for in vitro *electrophysiology.* Male mice (1–2.5 months old; *Hdc*-Cre;tdTom mice, *n* = 17; wild-type mice, *n* = 4) were deeply anesthetized with inhaled isoflurane, followed by an intraperitoneal injection of ketamine/xylazine, and transcardially perfused with 20 ml of ice-cold sucrose solution as follows (in mM): 87 NaCl, 75 sucrose, 25 glucose, 25 NaHCO₃, 7.5 MgCl₂, 2.5 KCl, 1.25 NaH₂PO₄, and 0.5 CaCl₂. Coronal brain slices (225 μm thick) were cut in ice-cold sucrose using a vibrating microtome (7000smz-2, Campden Instruments). Slices were allowed to recover for 45 min at 34°C in artificial CSF (ACSF) as follows (in mM): 125 NaCl, 25 NaHCO₃, 11 glucose, 2.5 KCl, 1.25 NaH₂PO₄, 1 MgCl₂, and 1 CaCl₂ (~305 mOsm/L). Slices were then transferred to room temperature for at least 30 min before recording. All solutions were bubbled with 95% O₂/5% CO₂.

Cell-attached and whole-cell recordings from slices. Cells were visualized with an upright Olympus BX51microscope (Olympus America Inc.) with infrared differential interference contrast and identified by tdTom expression with epifluorescence illumination. Slices were placed in the recording chamber and superfused with bubbled ACSF at physiological temperature (34–35°C), at which all recordings were performed. All recordings were acquired using a Multiclamp 700B amplifier and pClamp10 acquisition software (Molecular Devices; RRID:SCR_011323). In loose-seal, cell-attached patch (CAP) configuration, recordings were performed with ACSF in the pipette, and with low resistance seals (<50 MΩ), allowing minimal disruption to the cell. Upon obtaining a stable loose seal recording, we recorded for 5 min. If the cell was spontaneously active, we recorded for an additional 5 min to further confirm stable activity. Whole-cell voltage-clamp and current-clamp recordings were performed using an internal solution of the following composition (in mM): 130 K-gluconate, 10 HEPES, 0.1 EGTA, 10 NaCl, 2 MgCl₂, 10 phosphocreatine (tris), 4 Mg-ATP, and 0.3 Na-GTP (290 mOsm/L), pH 7.2. Tight seals of >1 GΩ were obtained before rupturing the membrane. Only recordings with a stable series resistance of <20 MΩ were included in the data analysis.

Biocytin staining and imaging. For cell fills, internal solutions contained 0.1% biocytin and cells underwent whole-cell recording for at least 10 min with the biocytin-based internal solution. After recording, slices were fixed in 4% PFA for 30 min and stored overnight in 0.5% Triton/PBS at 4°C. Slices were then incubated with streptavidin conjugated to Alexa Fluor 488 (1:500; Thermo Fisher Scientific; RRID:AB_2336881) for 2 h. After washing the sections four times, 10 min each, they were mounted onto slides with Vectashield with DAPI. Washes and incubations were performed in 0.5% Triton X-100 plus 5% DNS.

Analysis of slice electrophysiology data. All data were analyzed with ClampFit (Molecular Devices; RRID:SCR_011323) and MATLAB R2015a (MathWorks; RRID:SCR_001622). For CAP recordings, the firing rate, interspike interval (ISI), and coefficient of variation of the ISI (CVISI) were calculated based on a repeated 5-min-long recording of spontaneous activity. In voltage-clamp experiments, passive properties were determined from a 100 ms hyperpolarizing step of −5 mV, where the cell was initially held at a holding potential, V_h = −90 mV. Input resistance was calculated using the change in current 50 ms before the step and the last 50 ms during the step. Upon subtracting the holding current off-line, the integrated area under the transient from the same trace was used to determine membrane capacitance. Multiple sweeps were averaged to remove noise.

In current-clamp experiments, spike ratio and repolarization latency from active cells were initially obtained through 1 s hyperpolarizing steps. If the cell was not spontaneously active, current was injected to obtain a firing rate of 1–2 Hz. Spike ratio was calculated as the ratio of firing rate 1 s before and 250 ms after the step. Single action potential (AP) properties were determined from a 1 s depolarizing step, in which the cell was also held around V_h = −80 mV. The first evoked spike was used to extract action potential properties. Spike threshold was defined as the voltage at 2% of the maximum time derivative of the voltage (dV/dt). AP and afterhyperpolarization (AHP) amplitudes were measured from the peak and the trough of the AP waveform, relative to the threshold. Rise and decay times were also based on the threshold. AP half-width was defined at the midpoint between AP threshold and AP peak. Membrane potential values are corrected for a liquid junction potential of −10.2 mV, calculated using pClamp10. Statistical comparisons between classified groups (tdTom⁺/⁻ and HA⁺/⁻) was based on the nonparametric Mann–Whitney test due to the non-normality in a majority of the dataset across parameters (*p* < 0.05, Shapiro–Wilk W test). Statistical significance was determined as *p* < 0.05.

Unsupervised hierarchical cluster analysis. Cluster analysis was performed in R (R-Project for Statistical Computing; http://www.R-project.org/; RRID: SCR_001905). Each active and passive electrical property was standardized for comparison on a common scale. Euclidean distance was calculated to determine dissimilarity between cells and grouped cells, represented by the length of the branch. Clustering was based on the method of Ward (1963), minimizing within-group variance.

Surgery and recording for in vitro *optogenetics.* Male *Hdc*-Cre;tdTom mice (1.5 months old, *n* = 2) under inhaled isoflurane were injected with 700 nl of a Cre-dependent adeno-associated virus (AAV) encoding Arch3.0-enhanced yellow fluorescent protein (EYFP) under the CAG promoter (AAV5-CAG-FLEX-Arch3.0-EYFP) unilaterally in the ventrolateral TMN (anteroposterior, −2.4; ML, +0.75; DV, −5.4 mm) using a digital stereotactic apparatus (David Kopf Instruments). This viral vector was serotyped with AAV5 coat proteins and packaged by the Vector Core of the University of North Carolina, Chapel Hill (RRID:SCR_002448). The virus was injected at a rate of 50 nl/min. Slice electrophysiology experiments were performed over 3 weeks following viral injection. For *in vitro* photostimulation, slices were subject to whole-field illumination with green light (532 nm) using a transistor–transistor logic (TTL)-controlled white LED (TLED, Sutter Instrument), transmitted through an mCherry filter cube (Olympus America) and a 60× objective (Olympus America). For cell-attached and whole-cell recordings, cells were stimulated using either 1-s-long pulses or 1-min-long pulses. For voltage-clamp recordings, cells were held at V_h = −70 mV and subjected to 1-s-long pulses with varying light intensity using an arbitrary scale of 1–11: 25% (0.24 mW), 50% (0.50 mW), 75% (0.75 mW), and 100% (1.00 mW) as measured using a digital power meter (Thorlabs).

Surgery and implantations for in vivo *optogenetics.* Surgeries for *in vivo* optogenetics and polysomnography were performed on male *Hdc*-Cre mice (2 months old, *n* = 8) under ketamine/xylazine anesthesia injected intraperitoneally (100 and 10 mg/kg, respectively) and placed on a digital stereotactic apparatus (David Kopf Instruments). To selectively express Arch3.0-EYFP and control EYFP viral constructs in HA neurons of the TMN, we injected recombinant AAV (AAV5-CAG-FLEX-Arch3.0-EYFP or AAV5-CAG-FLEX-EYFP) bilaterally into the TMN (anteroposterior, −2.4; ML, ±0.75; DV, −5.4 mm). A volume of 600 nl of virus was injected into each hemisphere through a stainless steel 33 gauge injector cannula (Plastics One) connected to a 10 μl Hamilton syringe placed on a programmable precision pump (World Precision Instruments) at a rate of 100 nl/min. The cannula was left at the injection site for at least 15 min and slowly removed. After injections, mice were implanted with two optical fiber implants with the following characteristics: 200 μm diameter fiber, 0.22 numerical aperture, 6 mm length with a 1.25 mm diameter metal ferrule (Doric Lenses), connected together by glued zirconia sleeves that allow connections with fiber-optic patchcords (Doric Lenses). The distance between the two optical fiber implants could vary from 1.46 to 1.8 mm, center-to-center. Fiber implant placement (anteroposterior [AP], 2.46 to 2.8; mediolateral [ML], 0.73 to 0.9; dorsoventral [DV], 4.7 to 5.2 mm) are reported in Figure 6C. Fiber implants and

zirconia sleeves were affixed to the skull with C&B Metabond (Parkell) and dental acrylic. Mice were then equipped for electroencephalographic (EEG) and electromyographic (EMG) recording by implanting two gold-plated cortical EEG screw electrodes (EEG: anteroposterior, 1.5; ML, −1.5; EMG: anteroposterior, −3.5; ML, −2.8 mm) and two EMG wire electrodes (316SS/44T, Medwire) inserted between the neck musculature. Finally, the EEG/EMG electrodes, presoldered to a four-pin connector, were affixed to the skull with C&B Metabond and dental acrylic. We used surgical sutures to close the wound, and the mice were kept in a warm environment until resuming normal activity. Mice were allowed to recover for 2 weeks and then acclimated to a flexible EEG/EMG recording cable and optical patchcords for 7–10 d within individual Plexiglas recording chambers in custom-designed stainless steel cabinets at constant temperature (22 ± 1°C), humidity (40–60%), and circadian cycle (12 h light/dark cycle, lights on at 8:00 A.M.) with food and water available *ad libitum*. Each cable was flexible so that mice could move freely within the chamber.

In vivo *photostimulation, EEG/EMG recording, and sleep behavior.* All experiments took place between 7:00 and 10:00 P.M. at the end of the light cycle when mice enter their nocturnal active period with a minimum 3 d interval between sessions (five sessions total per control *Hdc*-Cre;EYFP mouse, and three sessions per *Hdc*-Cre;ArCh3.0-EYFP mouse). To induce optogenetic inhibition, photoillumination (532 or 594 nm) was delivered by diode-pumped solid-state laser systems (LaserGlow). For each animal, we calibrated the light power of the lasers such that the light power exiting the preimplanted optical fiber implants was set between 15 and 17 mW. Cortical EEG and EMG signals from neck muscles, derived from the surgically implanted electrodes, were amplified (Grass Technologies) and digitized at 256 Hz using sleep recording software (Vital Recorder, Kissei Comtec America). Using sleep analysis software (SleepSign for Animals, Kissei Comtec America), we digitally filtered the signal (EEG, 0.3–25 Hz; EMG, 25–50 Hz) and manually scored by 4 s epochs for wake, slow-wave sleep (SWS), and rapid eye movement sleep (REMS). Then raw data were extracted to apply fast Fourier transformation on the cortical EEG signals using MATLAB R2015a (MathWorks) during natural (no-light) wake and SWS in all mice and during the photoillumination period. To compare EEG spectra, the data were normalized using the root mean square (RMS) vector method. The EMG data were also rectified and smoothed using the RMS (RMS_{EMG}). RMS_{EMG} values were normalized to the corresponding values at prelight baseline stage to provide an estimation and comparison of the EMG amplitude in response to photoillumination. To synchronize EEG/EMG recording with photoillumination, a TTL signal was sent to the sleep acquisition software at the onset of light (delay, <100 ms). A baseline for natural sleep/wake behavior was recorded 48 h before the optogenetic experiment day on similar timing for 2 h between 7:00 and 10:00 P.M. On the optogenetic experiment day, EEG/EMG signals were recorded for a period of 1 h before and 1 h after photoillumination sessions. Continuous light was delivered for 5 min once the mouse displayed 2 min of sustained, active wakefulness.

Analysis of in vivo *optogenetic data.* We analyzed all data using Prism 7.0a (GraphPad Software; RRID:SCR_002798). Statistical significance was set at $p < 0.05$ for all procedures. Normality and homoscedasticity assumptions were verified before the use of any parametric tests. When these assumptions were not met, standard transforms were applied to meet the above criteria. Two-way repeated-measures ANOVA followed by multiple-comparison tests, Sidak's or Tukey's test, were performed to test the interaction between frequency bands and genotype/inhibition (control *Hdc*-Cre;EYFP and *Hdc*-Cre;Arch3.0-EYFP mice), time bins and genotype/inhibition, and postphotoillumination periods and genotype on sleep–wake parameters and EEG power densities, as well as the differences between each of these factors. In addition, Mann–Whitney tests were used to examine differences between RMS_{EMG} and SWS latencies and genotypes/inhibition. Data are presented as the mean ± SEM. Quantitative changes in EEG power were analyzed for delta (0.5–4.25 Hz), theta (4.3–9.75 Hz), alpha/gamma/low-beta (9.9–19 Hz), and high-beta/low-gamma (>20 Hz: 20–30 Hz) frequency bands. For the preparation of the figures, we used MATLAB R2015a and Prism 7.0a and then exported the data into Illustrator CS6 (Adobe Systems; RRID:SCR_014198).

Results
Whole-brain distribution of tdTom^{+} neurons in *Hdc*-Cre;tdTom mice

Classical neuroanatomical studies have demonstrated that HDC-expressing HA neurons in the adult rodent brain are exclusively found in the posterior hypothalamus, concentrated in the TMNv (Watanabe et al., 1983, 1984; Hayashi et al., 1984; Wouterlood et al., 1986; Ericson et al., 1987; Bayliss et al., 1990; Castrén and Panula, 1990; Karlstedt et al., 2001; Parmentier et al., 2002). To achieve cell type-specific genetic manipulation of HA neurons, two previously described cre-recombinase driver lines have been generated using the *Hdc* promoter. Yanovsky et al. (2012) described a BAC transgenic HDC-Cre driver line with high specificity and moderately high penetrance of cre expression in the TMNv region on the basis of lacZ-IR and HDC-IR (Yanovsky et al., 2012) but with some scattered cre expression in the thalamic dorsolateral geniculate nucleus (DLG) and posterior thalamic nuclei (Walker et al., 2013). This line was used in subsequent optogenetic experiments reporting photostimulation-evoked HA release by HA neurons (Williams et al., 2014). Zecharia et al. (2012) reported a knock-in cre line (HDC-Cre), and using cre-dependent lacZ expression, they found labeled cells enriched in the TMNv, as expected. However, labeled cells were also found in other brain regions, including ependymal cells lining the ventricles, DLG and other thalamic nuclei, as well as some labeled cells in the hypothalamus, brainstem, and cerebellum, which the authors posit may reflect transient expression of the *Hdc* gene during embryonic development (Zecharia et al., 2012), in part based on previous developmental gene expression data in the mouse (Karlstedt et al., 2001). This line was subsequently used for conditional genetic manipulations (Zecharia et al., 2012; Yu et al., 2014; Uygun et al., 2016) and chemogenetic and optogenetic activation experiments (Yu et al., 2015). A third cre driver line, a BAC transgenic *Hdc*-Cre mouse, was generated as part of the GENSAT Project (Gong et al., 2003, 2007), and described in online databases from GENSAT (http://gensat.org) and the Allen Brain Institute (http://connectivity.brain-map.org/; Harris et al., 2014) but has yet to be fully validated and characterized.

We first evaluated the specificity and penetrance of cre-mediated recombination in TMNv HA neurons in the whole brain of *Hdc*-Cre mice. To examine the whole-brain distribution of recombined cells in this line, we crossed it to Ai14, a reporter line that expresses the red fluorescent protein tdTomato (tdTom) following cre-mediated recombination (Madisen et al., 2010). Both parasagittal and coronal sections were obtained from adult *Hdc*-Cre;tdTom mice, and fluorescent images of whole-brain sections were acquired. In parasagittal and coronal sections, *Hdc*-Cre;tdTom mice exhibited selective tdTom expression in the posterior hypothalamus, concentrated along the ventral edge of the TMN (Fig. 1 *A*, *B*), consistent with the well described distribution of HA neurons in the rodent brain. *Hdc*-Cre;tdTom mice exhibited minimal tdTom expression outside of the TMN (Fig. 1 *A*, *B*). We found little to no detectable tdTom labeling in the thalamus, other regions of the hypothalamus, or ependymal cells, but we did find a few scattered small cell bodies and very sparse fibers in the cerebellar cortex and cerebellar nuclei. Therefore, at the whole-brain level, we observed that tdTom labeling in *Hdc*-Cre;tdTom mice is confined to the TMN with minimal extra-TMN expression, consistent with the distribution of *Hdc*-expressing neurons in the adult rodent brain.
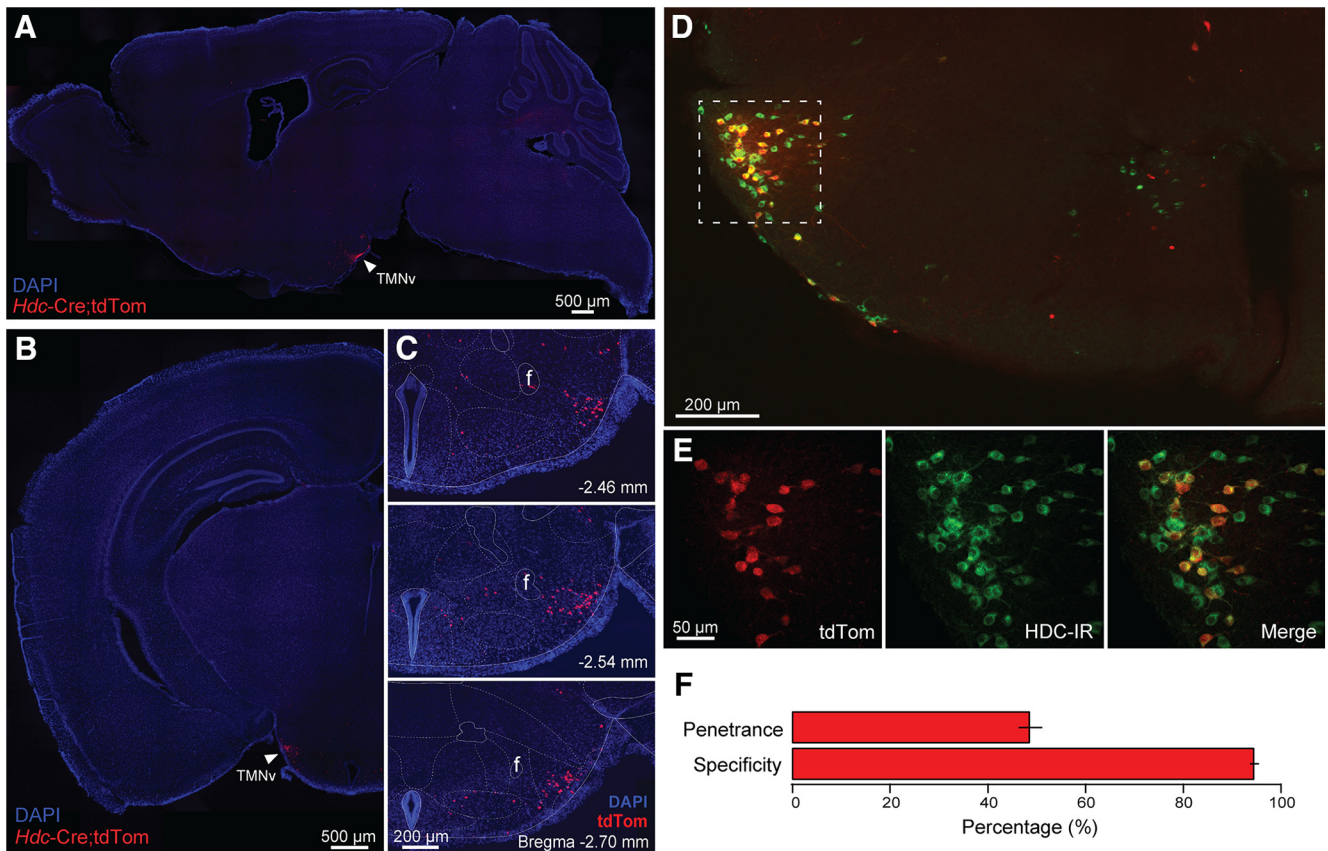
Figure 1. Neuroanatomical characterization of *Hdc*-Cre transgenic mice. *A*, *B*, Whole-section fluorescent photomicrographs of *Hdc*-Cre;tdTom mouse brains at the level of the TMNv (arrows) in 10× stitched parasagittal (*A*) and coronal (*B*) sections. Red, tdTom expression mediated by cre-mediated recombination; blue, DAPI. *C*, Serial coronal sections of the TMN in *Hdc*-Cre;tdTom mice proceeding from anterior (top) to posterior (bottom) as indicated by distance from bregma, 10× stitched; "f" denotes fornix. *D*, Representative coronal section of the TMN from an *Hdc*-Cre;tdTom mouse, immunostained with anti-HDC, 10× stitched. Area of higher magnification indicated by the dashed white box. *E*, Confocal photomicrographs at 40× of the TMNv in a selected region from *D* displaying expression of tdTom (left), HDC-IR (middle), and merged (right). *F*, Summary of quantification of cells from all sections measuring specificity (%tdTom$^+$ cells that are HDC-IR) and penetrance (%HDC-IR cells that are tdTom$^+$) of cre recombinase expression in TMNv HA neurons. Error bars represent ± SEM.

Specificity and penetrance of cre-mediated recombination in TMN HA neurons in *Hdc*-Cre;tdTom mice

Having established that cre-mediated recombination is limited to the region of the TMN in *Hdc*-Cre;tdTom mice, we next examined the distribution of tdTom$^+$ cells within the TMN itself and determined how faithfully they report the expression of HDC. We first took serial sections through the rostrocaudal extent of the TMN (Fig. 1C) and found that tdTom$^+$ cells were distributed in a pattern broadly consistent with HA-IR neurons in the rat (Panula et al., 1984) and mouse (Parmentier et al., 2002), and with HDC-IR neurons in the rat (Ericson et al., 1987). tdTom$^+$ cell bodies were found scattered in the ventral portion of the posterior hypothalamus but more densely packed in the TMNv, as expected (Fig. 1C).

We next determined the specificity and penetrance of cre-mediated recombination in HA neurons of the TMNv in *Hdc*-Cre;tdTom mice. For this purpose, we performed HDC immunohistochemistry on *Hdc*-Cre;tdTom coronal brain sections and quantified tdTom labeling (red) relative to HDC immunoreactivity, visualized with Alexa Fluor 488 (green), in single neurons in the TMNv. To visualize tdTom expression and HDC immunoreactivity, we acquired stitched fluorescent images of the whole posterior hypothalamus at 10× (Fig. 1D) followed by confocal imaging of the TMNv at 40× (Fig. 1E). A total of 1894 cells were analyzed from 47 sections (n = 3 mice). Specificity of cre recombination was defined as the percentage of tdTom$^+$ cells

that were also HDC-IR. We found that 94.7% of tdTom$^+$ cells in the TMNv were HDC-IR, indicating that the expression of cre in *Hdc*-Cre;tdTom mice is highly specific to HDC-expressing cells (Fig. 1F). Penetrance of cre recombination was defined as the percentage of HDC-IR cells that were also tdTom$^+$. Our analysis revealed that 48.8% of HDC-IR cells in the TMNv were tdTom$^+$, indicating that approximately half of HDC-IR HA neurons in the TMNv are capable of cre-mediated recombination (Fig. 1F). We observed rare, scattered tdTom$^+$ cells in the posterior hypothalamus that did not appear to be HDC-IR and vice versa. Together, these data indicate that *Hdc*-Cre mice specifically allow cre-mediated recombination in HA neurons of the TMNv, with low/moderate penetrance but high specificity and minimal extra-TMN expression.

Unsupervised classification of TMNv HA$^+$ and HA$^-$ neurons based on characteristic membrane properties in *Hdc*-Cre; tdTom mice

We next performed a comprehensive analysis of the membrane properties of genetically labeled HA neurons and unlabeled non-HA neurons within the TMNv region of *Hdc*-Cre;tdTom transgenic mice to quantitatively determine their electrophysiological diversity. HA cells were identified based on tdTom expression (tdT$^+$) and their location within the TMNv in brain slices relative to defining anatomical landmarks, similar to the recording sites illustrated in Figure 2A. All neurons were systematically
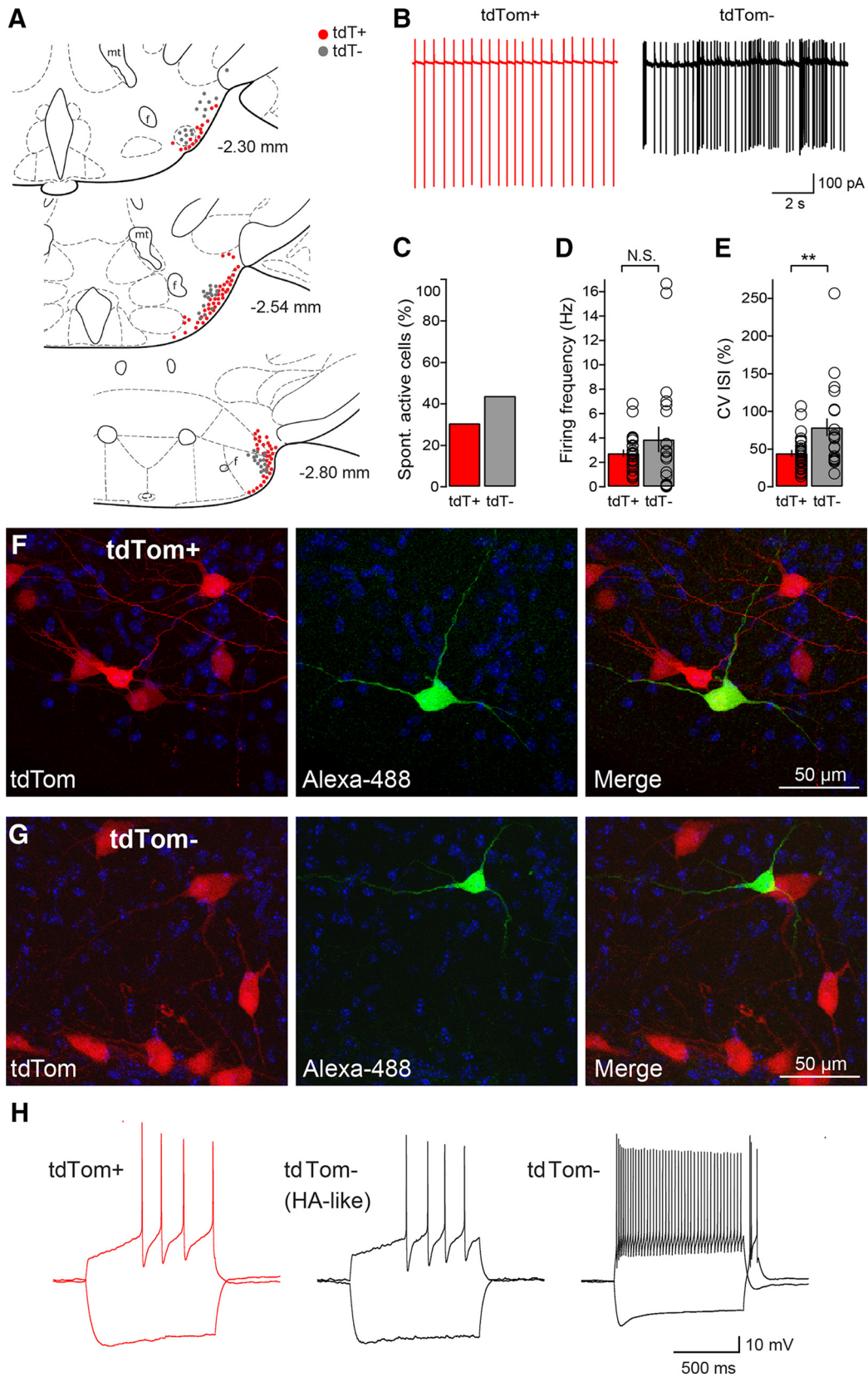
Figure 2. Cell-attached and whole-cell recordings from tdTom[+] and tdTom^{−} cells in the TMNv of *Hdc*-Cre;tdTom mice. *A*, Schematic illustrating anatomical location and identity of TMNv neurons recorded using loose-seal cell-attached patch [tdTom[+] (in red), 88 cells; tdTom[−] (in gray), 48 cells]. *B*, Representative traces of tdTom[+] and tdTom^{−} cells in loose-seal cell-attached patch configuration. *C–E*, Bar plots representing the percentage of spontaneously active cells in both groups (*C*), firing rates (*D*), and CVISI (*E*) between tdTom[+] and tdTom^{−} cells. Asterisks indicate statistical significance: **$p < 0.01$. N.S., Not significant. *F*, Representative confocal photomicrographs of a biocytin-filled tdTom[+] neuron with tdTom expression (left), biocytin-filled neuron immunostained with streptavidin conjugated to Alexa Fluor 488 (middle) and merged image (right). *G*, Representative confocal photomicrograph of a tdTom[−] neuron. *H*, Representative traces of whole-cell recordings from tdTom[+] and tdTom^{−} neurons held at −80 mV and subjected to 1-s-duration hyperpolarizing and depolarizing steps of ±60 pA.
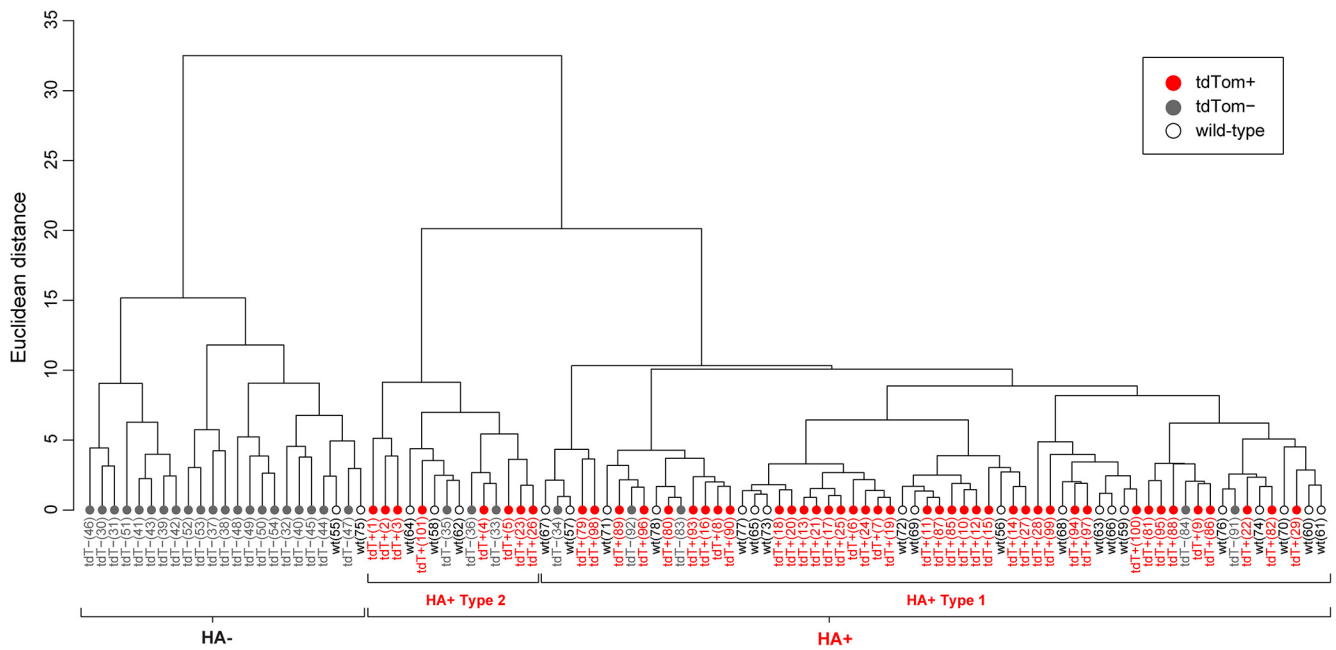
Figure 3. Unsupervised hierarchical cluster analysis of TMNv HA $^+$ and HA $^-$ neurons based on membrane properties. Dendrogram of unsupervised cluster analysis depicting two distinct, major clades based on 17 passive and active membrane properties using the method of Ward (1963). Properties: capacitance, time constant, input resistance, maximum dV/dt, AP threshold, AP peak, AP amplitude, AHP amplitude, AP trough, AP half-width, 10–90% rise time, 90–10% decay time, maximum firing rate, repolarization latency, spike ratio, sag ratio, and gain. The predominantly tdTom $^-$ clade (left) is referred to as HA $^-$, and the largely tdTom $^+$ clade (right) is referred to as HA $^+$. Note the dichotomy within the HA $^+$ clade, referred to as HA $^+$ Type 1 (right) and Type 2 (right).

subjected to the same experimental procedures and analysis routines, which are described in the following sections.

Previous work has shown that putative HA neurons fire spontaneously *in vitro*, but differences may be attributable to the use of different species, tissue preparation, recording method, temperature, and other conditions (Haas and Reiner, 1988; Weiss et al., 1989; Llinás and Alonso, 1992; Stevens and Haas, 1996; Stevens et al., 2001). Therefore, we began by recording from TMNv neurons using loose-seal, cell-attached patch configuration at physiological temperature to determine spontaneous firing rate and pattern in the absence of synaptic blockers. To ensure an accurate survey of neurons within the region of the TMNv, we noted the location of each recorded cell and mapped it onto a standardized neuroanatomical atlas (Paxinos and Franklin, 2012; Fig. 2A). We found that 31% of tdTom $^+$ cells (27 of 88 cells) and 44% of tdTom $^-$ cells (21 of 48 cells) exhibited spontaneous activity (Fig. 2C), with representative examples shown in Figure 2B. Among neurons that were spontaneously active, the average firing rate of tdTom $^+$ cells was 2.75 ± 0.28 Hz (mean ± SEM), while that of tdTom $^-$ cells was slightly higher at 3.89 ± 1.05 Hz (Fig. 2D), although there was no significant difference between the two ($p = 0.79$). We also determined the regularity of firing using the CVISI. Spontaneously active tdTom $^+$ neurons had a CVISI of 44.4 ± 4.4%, while tdTom $^-$ neurons had a significantly higher CVISI of 79.1 ± 11.9% ($p < 0.01$; Fig. 2E), exemplified by the irregular firing pattern of the tdTom $^-$ cell shown in Figure 2B. These data suggest that while both cell populations have a proportion of neurons that are spontaneously active at low firing rates, tdTom $^+$ neurons have a tendency to exhibit a more regular, rhythmic firing pattern than tdTom $^-$ neurons.

Upon obtaining whole-cell configuration, we evaluated the passive and active properties of tdTom $^+$ ($n = 48$) and tdTom $^-$ neurons ($n = 29$) in *Hdc*-Cre;tdTom transgenic mice. To control for the possibility that the membrane properties of TMNv neu-

rons may be altered in these transgenic mice, we also recorded from putative HA neurons in wild-type mice with a C57BL/6 background ($n = 24$), identified based on their location within the TMNv. Some cells were filled with biocytin and resolved with streptavidin-Alexa Fluor 488 to confirm the absence or presence of tdTom (Fig. 2F,G). We subjected each cell to a comprehensive battery of voltage-clamp and current-clamp protocols (see Materials and Methods) and noticed striking differences between intermingled tdTom $^+$ and tdTom $^-$ neurons, exemplified by the representative current-clamp recordings in which cells are held at −80 mV and undergo depolarizing and hyperpolarizing steps of ± 60 pA (Fig. 2H). While tdTom $^+$ neurons all exhibited a pronounced latency to firing following a depolarizing step, td-Tom $^-$ neurons typically exhibited a burst or a rapid increase in firing rate with a depolarizing step, and often a rebound burst immediately following a hyperpolarizing step. However, a small minority of tdTom $^-$ neurons displayed the features of tdTom $^+$ neurons that we referred to as HA-like.

While broadly consistent with the characteristics of HA neurons described by Llinás and Alonso (1992) using sharp microelectrodes in guinea pig slices, we wished to systematically evaluate the heterogeneity of membrane properties of TMNv neurons using multiple parameters. To accomplish this, we measured and analyzed a total of 17 passive and active membrane properties in each cell and used unsupervised hierarchical clustering using the method of Ward (1963) to identify distinct groups among the tdTom $^+$ and tdTom $^-$ cells. The resulting dendrogram is shown in Figure 3 with Euclidean distance, as a measure of dissimilarity, shown in the vertical axis. This classification resulted in two distinct clades at the first branch point, one composed of tdTom $^-$ cells from *Hdc*-Cre;tdTom mice ($n = 21$ of 23) and a few wild-type cells ($n = 2$ of 23), and another larger clade primarily composed of tdT $^+$ cells (48 of 78) along with several tdTom $^-$ (8 of 78) from *Hdc*-Cre;tdTom mice and wild-type cells

Table 1. Passive and active membrane properties of TMNv HA $^+$ and HA $^-$ neurons

	HA $^+$ (n = 78)		HA $^-$ (n = 23)		
	Mean	SEM	Mean	SEM	p value
Passive membrane properties					
Capacitance (pF)	42.27	1.19	27.10	2.40	<0.0001*
Time constant (ms)	33.86	1.36	33.45	3.45	0.4887
Input resistance (MΩ)	459.91	17.78	770.86	112.49	0.0576
Resting membrane potential (mV)	−69.40	0.68 (n = 50)	−71.41	1.85 (n = 14)	0.2263
Active membrane properties					
Maximum dV/dt (mV/ms)	146.13	4.57	234.99	15.96	<0.0001*
AP threshold (mV)	−43.90	0.36	−53.63	0.66	<0.0001*
AP peak (mV)	23.41	0.65	10.41	1.29	<0.0001*
AP amplitude (mV)	67.31	0.59	63.81	1.49	0.0179*
AHP amplitude (mV)	26.60	0.33	18.13	0.95	<0.0001*
AP trough (mV)	−70.50	0.48	−71.52	0.86	0.2007
AP half-width (ms)	1.81	0.07	0.72	0.06	<0.0001*
10–90% rise (ms)	0.60	0.03	0.36	0.03	<0.0001*
90–10% decay (ms)	1.67	0.07	0.60	0.06	<0.0001*
Maximum firing (Hz)	28.90	1.31	106.74	17.62	<0.0001*
Repolarization latency (at −60 pA)	1496.46	130.58	129.08	58.76	<0.0001*
Spike ratio	0.03	0.02	6.16	1.05	<0.0001*
Sag ratio (at −60 pA, %)	0.95	<0.01	0.95	0.01	0.7005
Gain	0.10	<0.01	0.58	0.07	<0.0001*

*Statistical significance with $p < 0.05$ across groups based on the Mann–Whitney test.

(22 of 78). This result confirmed that all of the tdTom $^+$ neurons that we recorded from exhibited a set of common features that were consistent with their identity as HA neurons and further confirmed the anatomical specificity (94.7%) of this transgenic line. At the same time, given its low/moderate penetrance (48.8%), we were unsurprised to find a number of unlabeled, tdTom $^-$ cells that also exhibited the electrophysiological hallmarks of HA neurons and were functionally indistinguishable from labeled cells. For this reason, we operationally defined the former clade as HA $^-$ (n = 23) and the latter as HA $^+$ (n = 78) for the remainder of the *in vitro* analysis. Furthermore, we recorded from 24 wild-type TMNv neurons and found that 92% of them (22 of 24 neurons) were evenly distributed among the HA $^+$ neuron clade, confirming that putative HA neurons in *Hdc*-Cre; tdTom transgenic mice exhibit unaltered membrane properties compared with wild-type neurons. Finally, we also observed that the properties of HA $^+$ neurons could be further parsed into two major subclades (HA $^+$ Types 1 and 2) as shown in Figure 3, a dichotomy that suggests diversity among HA $^+$ neurons. A quantitative comparison of the membrane properties of HA $^+$ and HA $^-$ neurons is found in Table 1, along with an illustration of key electrical signatures in Figure 4. A comparison of HA $^+$ Type 1 and 2 cells is found in Table 2 and described in more detail in the following section.

Characteristic passive and active membrane properties that distinguish TMNv HA $^+$ and HA $^-$ neurons, and diversity among HA $^+$ neurons, in *Hdc*-Cre;tdTom mice

We next performed a detailed comparison of TMNv HA $^+$ and HA $^-$ neurons. Among the passive membrane properties that we measured (Table 1), capacitance stood out as being the only significantly different parameter between HA $^+$ and HA $^-$ neurons. We found that HA $^+$ neurons had a significantly larger capacitance (42.27 ± 1.19 pF) than HA $^-$ neurons (27.10 ± 2.40 pF; $p <$ 0.0001), which is consistent with the appearance of larger-diameter cell bodies among HA $^+$ neurons (Fig. 2F), although the membrane time constants are similar. In addition, both neuron populations exhibit high input resistance values, with HA $^-$ neurons (770.86 ± 112.49 MΩ) having generally higher, though not

statistically significant, input resistance than HA $^+$ neurons (459.91 ± 17.78 MΩ). In current-clamp mode, only 30–40% of cells were found to be spontaneously active in each group, and the silent cells have similar resting membrane potential values of −69.40 ± 0.68 mV (HA $^+$; n = 50/78 cells) and −71.41 ± 1.85 mV (HA $^-$; 14/23 cells).

HA $^+$ and HA $^-$ neurons display dramatically different active membrane properties in response to depolarizing current injections (Fig. 4A–F). To compare active properties across cells, membrane potential (V_m) was held at −80 mV and 1 s depolarizing steps of +20 pA were applied until cells reached a state of depolarization block. Representative traces of an HA $^+$ cell and an HA $^-$ cell are shown in Figure 4A, along with a corresponding plot of instantaneous frequency as a function of various current injections in Figure 4B. With increasing depolarizing steps, HA $^+$ neurons show the characteristically long latency to first spike, followed by a gradual increase in firing rate, while HA $^-$ cells typically display either a burst or a very high instantaneous firing rate before plateauing. Overall, HA $^+$ neurons display only a very shallow increase in firing frequency relative to HA $^-$ neurons, quantified as gain (Hz/pA). HA $^-$ neurons exhibit a highly variable but significantly greater gain than HA $^+$ neurons (Fig. 4C). In comparing single APs, HA $^+$ cells in our recordings show significantly longer AP half-widths (1.81 ± 0.07 ms) relative to HA $^-$ cells (0.72 ± 0.06 ms) along with slower rise and decay times ($p <$ 0.0001 for all three parameters). Overall, these results are consistent with previous descriptions of broad APs and shoulder-like repolarization phases (Haas and Reiner, 1988; Stevens et al., 2001; Haas and Panula, 2003), which were found to be calcium dependent and enhanced by repetitive firing (Llinás and Alonso, 1992). In addition, HA $^+$ neurons have significantly more depolarized AP thresholds and deeper AHPs than HA $^-$ cells ($p <$ 0.0001 for both parameters; Fig. 4D,E). Furthermore, the dichotomy in the firing properties of HA $^+$ and HA $^-$ neurons is illustrated in the relationship between maximal firing rate and AP half-width, where the broad APs of HA $^+$ neurons are strongly correlated with extremely slow firing rates. Of note, HA $^+$ Type 2 neurons exhibit the broadest APs and lowest firing rates among HA $^+$ neurons (Fig. 4F;
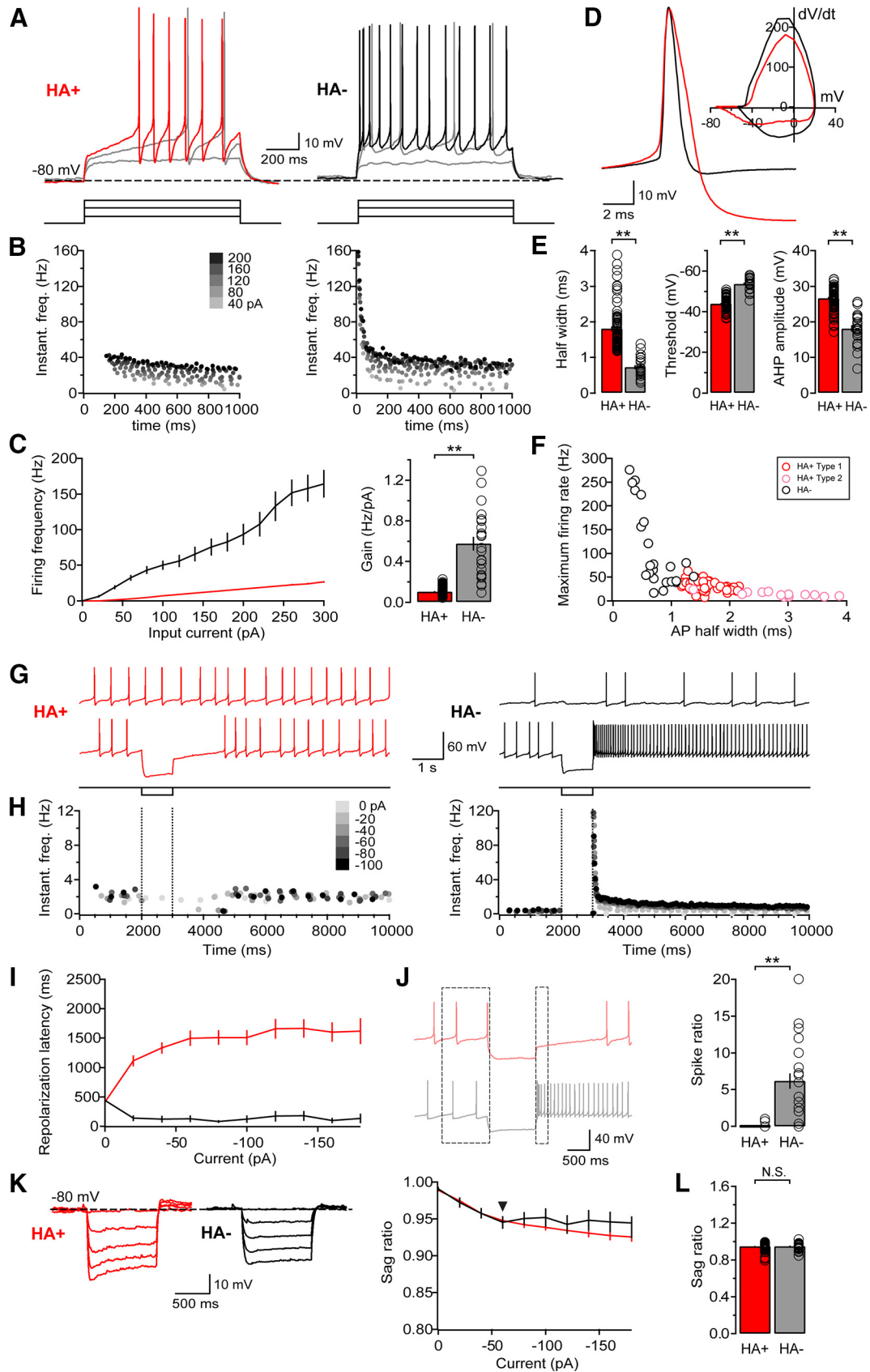
Figure 4. Key active membrane properties that distinguish TMNv HA $^+$ and HA $^-$ neurons. ***A***, Representative current-clamp responses of HA $^+$ (left) and HA $^-$ (right) neurons to three 1-s-long depolarizing current steps of $+20$ pA. ***B***, Corresponding instantaneous frequency plot of neurons shown in ***A*** in increasing steps of $+20$ pA until depolarization block. ***C***, Firing frequency (in Hz) as a function of input current (in pA) between HA $^+$ and HA $^-$ cells (left). Gain values quantified as the slope of the voltage response of each cell from $+40$ to $+140$ pA in $+20$ pA steps (right). ***D***, Single AP waveforms and the respective phase-plane plot extracted from the representative traces shown in ***A***. Waveforms are aligned to the time of the peak and the threshold value of the representative HA $^+$ cell for visualization purposes. ***E***, Bar plots of average and individual values of AP half-width (left), threshold (middle), and AHP amplitude (right) (*Figure legend continues.*)

Table 2. Passive and active membrane properties of TMNv HA $^+$ Type 1 and Type 2 neurons

	HA $^+$ Type 1 ($n = 64$)		HA $^+$ Type 2 ($n = 14$)		
	Mean	SEM	Mean	SEM	p value
Passive membrane properties					
Capacitance (pF)	42.57	1.34	40.91	2.64	0.4942
Time constant (ms)	31.08	1.29	46.59	3.06	0.0001*
Input resistance (MΩ)	429.91	16.46	597.06	51.56	0.0011*
Resting membrane potential (mV)	−69.92	0.67 ($n = 41$)	−67.06	2.17 ($n = 9$)	0.1187
Active membrane properties					
Maximum dV/dt (mV/ms)	158.49	3.94	89.62	6.65	<0.0001*
AP threshold (mV)	−43.92	0.38	−43.81	1.03	0.6162
AP peak (mV)	23.23	0.72	24.26	1.55	0.6580
AP amplitude (mV)	67.14	0.68	68.08	1.18	0.6533
AHP amplitude (mV)	27.47	0.26	22.65	0.82	<0.0001*
AP trough (mV)	−71.39	0.47	−66.46	1.01	0.0002*
AP half-width (ms)	1.58	0.03	2.87	0.17	<0.0001*
10−90% rise (ms)	0.51	0.01	1.01	0.07	<0.0001*
90−10% decay (ms)	1.45	0.04	2.69	0.16	<0.0001*
Maximum firing (Hz)	32.22	1.24	13.71	1.22	<0.0001*
Repolarization latency (at −60 pA)	1475.03	154.44	1594.41	182.65	0.1360
Spike ratio	0.04	0.02	0		0.4230
Sag ratio (at −60 pA, %)	0.96	<0.01	0.91	0.02	0.0019*
Gain	0.10	<0.01	0.11	0.01	0.9325

*Statistical significance with $p < 0.05$ across groups based on the Mann–Whitney test.

Table 2). In contrast, the exceptionally narrow APs of HA $^-$ neurons permit very high maximal firing rates (Fig. 4F).

Hyperpolarizing steps also revealed key membrane properties that distinguish HA $^+$ and HA $^-$ neurons from one another, as shown in Table 1 and illustrated in Figure 4G–L. In representative HA $^+$ and HA $^-$ neurons, hyperpolarizing current steps of −20 pA (one step of −60 mV is shown in Fig. 4G) were applied for 1 s duration to show responses to anode break, quantified in plots of instantaneous frequency (Fig. 4H). On anode break, all HA $^+$ cells show a delay to the first spike, while HA $^-$ neurons typically exhibit a rebound burst immediately following anode break. This phenomenon is shown as an increase in repolarization latency with increasing hyperpolarization in HA $^+$ cells (Fig. 4I) and reflected by a significant difference in spike ratio compared with HA $^-$ cells (Fig. 4J). In addition, we examined voltage sag, quantified as sag ratio, which we found to be relatively modest in both HA $^+$ and HA $^-$ neurons and not significantly different from each other during a hyperpolarizing step of −60 pA (Fig. 4K,L; Table 1). These properties of HA $^+$ neurons are broadly consistent with classical observations concerning the membrane properties of HA neurons in both rat and guinea pig brain slices, using sharp microelectrode recording (Haas and Reiner, 1988; Greene et al., 1990; Schönrock et al., 1991; Llinás and Alonso, 1992; Stevens and Haas, 1996). In particular, the pronounced latency to firing is best explained by the presence of a prominent A-type potassium

current in HA neurons, while the voltage sag is attributable to the hyperpolarization-activated cation current, described in rats, guinea pigs, and mice (Greene et al., 1990; Kamondi and Reiner, 1991; Llinás and Alonso, 1992; Jackson and Bean, 2007).

Furthermore, within the HA $^+$ group, two distinct subclades emerged, HA $^+$ Type 1 ($n = 64$) and HA $^+$ Type 2 ($n = 14$), and additional statistical analysis was performed on these types to define differences in their membrane properties (Table 2). Although both types exhibit the same general characteristics that distinguish them from HA $^-$ neurons, including broad APs and long repolarization latencies, key differences are apparent. Among passive membrane properties, HA $^+$ Type 1 neurons exhibit significantly lower input resistance values and lower membrane time constants than HA $^+$ Type 2 neurons. Several firing and single AP properties were also significantly different between the two types. Among other characteristics, HA $^+$ Type 1 neurons display significantly greater AHP amplitudes, shorter AP half-widths, faster rise and decay times, and higher maximum firing rates. These data suggest an unexpected diversity among the membrane properties of HA neurons within the TMNv.

Optogenetic inhibition of Arch3.0-expressing HA neurons in brain slices

We went on to characterize the effect of optogenetic silencing on the excitability of HA neurons in brain slices. Cell-attached patch and whole-cell recordings were obtained from labeled HA neurons in *Hdc*-Cre;tdTom mice, stereotactically injected with AAV5-CAG-FLEX-Arch3.0-EYFP in the TMNv. HA cells were identified by their expression of tdTom and location within the TMNv, as previously described, with whole-field green light (532 nm) illumination provided by a TTL-controlled LED. In voltage-clamp recordings, 1 s pulses of green light produced a light intensity-dependent outward current, maximal with ~1 mW (Fig. 5A). In cell-attached patch, reflecting the least perturbed recording configuration, 1 s pulses (~1 mW) led to complete silencing of spontaneous firing, which returned after a characteristic latency (Fig. 5B). In current-clamp recordings, green light pulses hyperpolarized the membrane potential causing complete cessation of firing (Fig. 5B) across multiple individual recordings, indicated

←

(*Figure legend continued.*) of HA $^+$ and HA $^-$ neurons. *F*, Scatterplot of maximum firing rate as a function of AP half-width of HA $^+$ and HA $^-$ cells, with HA $^+$ Type 1 (red) distinguished from HA $^+$ Type 2 (pink). *G*, Representative current-clamp traces of responses to hyperpolarizing steps of 0 and −60 pA for 1 s of HA $^+$ (left) and HA $^-$ (right) neurons. *H*, Corresponding instantaneous frequency plots of neurons from *G*. *I*, Average repolarization latency (time to first spike following anode break) as a function of hyperpolarizing current injection. *J*, Spike ratio values (right) calculated as the ratio of spikes before and after a current step of −60 pA as illustrated (left). *K*, Representative voltage-clamp responses to a series of hyperpolarizing current steps of −20 pA for 1 s in cells held at −80 mV (left). Sag ratio, defined as the ratio between peak and steady state, as a function of hyperpolarizing current steps (right) with the arrow indicating the response to a step of −60 pA. *L*, Bar plots of average and individual values of sag ratio measured at −60 pA. Asterisks indicate statistical significance **$p < 0.01$. N.S., Not significant.

by the raster plots and frequency histogram (Fig. 5C). Under these conditions, the photoillumination-induced hyperpolarization was similar in magnitude to the application of a modest 1 s hyperpolarizing current injection in the same cell (Fig. 5D). A longer-lasting (1 min) continuous light pulse, more similar to *in vivo* photoillumination conditions, also produced a relatively stable hyperpolarization of the membrane potential and complete silencing, which reversed following removal of the light (Fig. 5E).

Optogenetic silencing of HA neurons promotes slow-wave sleep in behaving mice

To test whether the silencing of HA neuron activity is sufficient to initiate sleep, or merely to impair wakefulness, in awake and behaving mice, we bilaterally injected AAV vector containing Arch3.0 (AAV5-CAG-FLEX-Arch3.0-EYFP) or EYFP alone (AAV5-CAG-FLEX-EYFP) expressed in a cre-dependent manner into the TMNv of *Hdc*-Cre mice. Robust cell-surface expression of Arch-EYFP is observed in HA neurons (Fig. 6A). We next analyzed polysomnographic recordings of *Hdc*-Cre; Arch3.0-EYFP (*n* = 5) and control *Hdc*-Cre;EYFP (*n* = 3) mice chronically implanted with cortical EEG and EMG electrodes, and bilateral optical fiber implants for photoillumination of the TMN (Fig. 6B). We verified that optical fiber placement accurately targets the TMNv throughout its rostrocaudal extent with ±250 μm dorsoventral and ±85 μm mediolateral differences between the fiber tips (Fig. 6C).

Optogenetic experiments were performed at the end of the light, inactive period (7:00 to 10:00 P.M., lights off at 8:00 P.M.) so that the circadian and homeostatic contributions to sleep remain minimal. Photoillumination sessions started when mice exhibited stable wakefulness, characterized by long bouts of wakefulness of at least 2 min marked by high EMG activity and low EEG slow-wave activity (SWA: 0.5–4.25 Hz oscillations). We first observed that sustained (5 min) green light photoillumination of Arch3.0-expressing HA neurons evokes increased EEG SWA within the first few minutes of lights on with concomitant reduced EMG activity (Fig. 6D). Changes in the EEG are marked by gradual emergence of large-amplitude slow oscillations and higher delta power (evident in the heat map plots of FFT power spectrum), compared with time-of-day equivalent wake–active behavior in control *Hdc*-Cre;EYFP mice (Fig. 6Di–Diii). To define this light-induced behavioral change, we first compared EEG power spectra of both control *Hdc*-Cre;EYFP and *Hdc*-Cre;Arch3.0-EYFP transduced mice during baseline, just before photoillumination tests when the animal is awake and during the 5 min of green light photoillumination (Fig. 6E). The wake baseline cortical EEG power spectra of *Hdc*-Cre;Arch3.0-EYFP transduced mice are not different from *Hdc*-Cre;EYFP control animals with the ex-
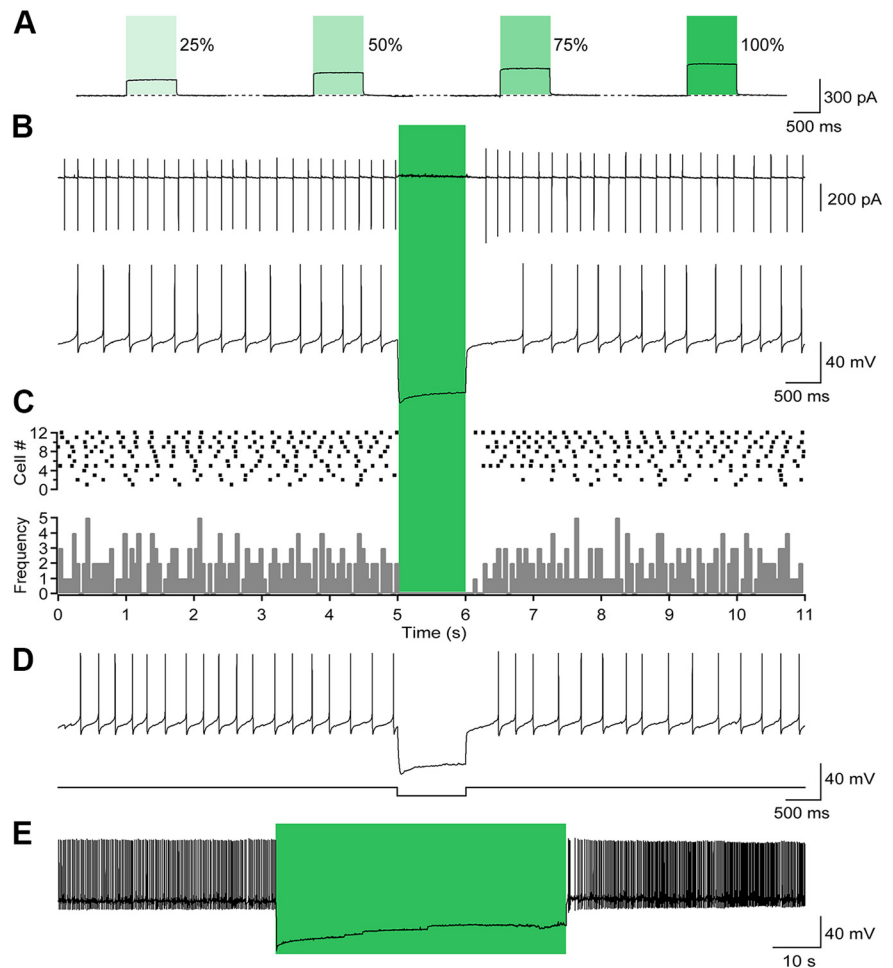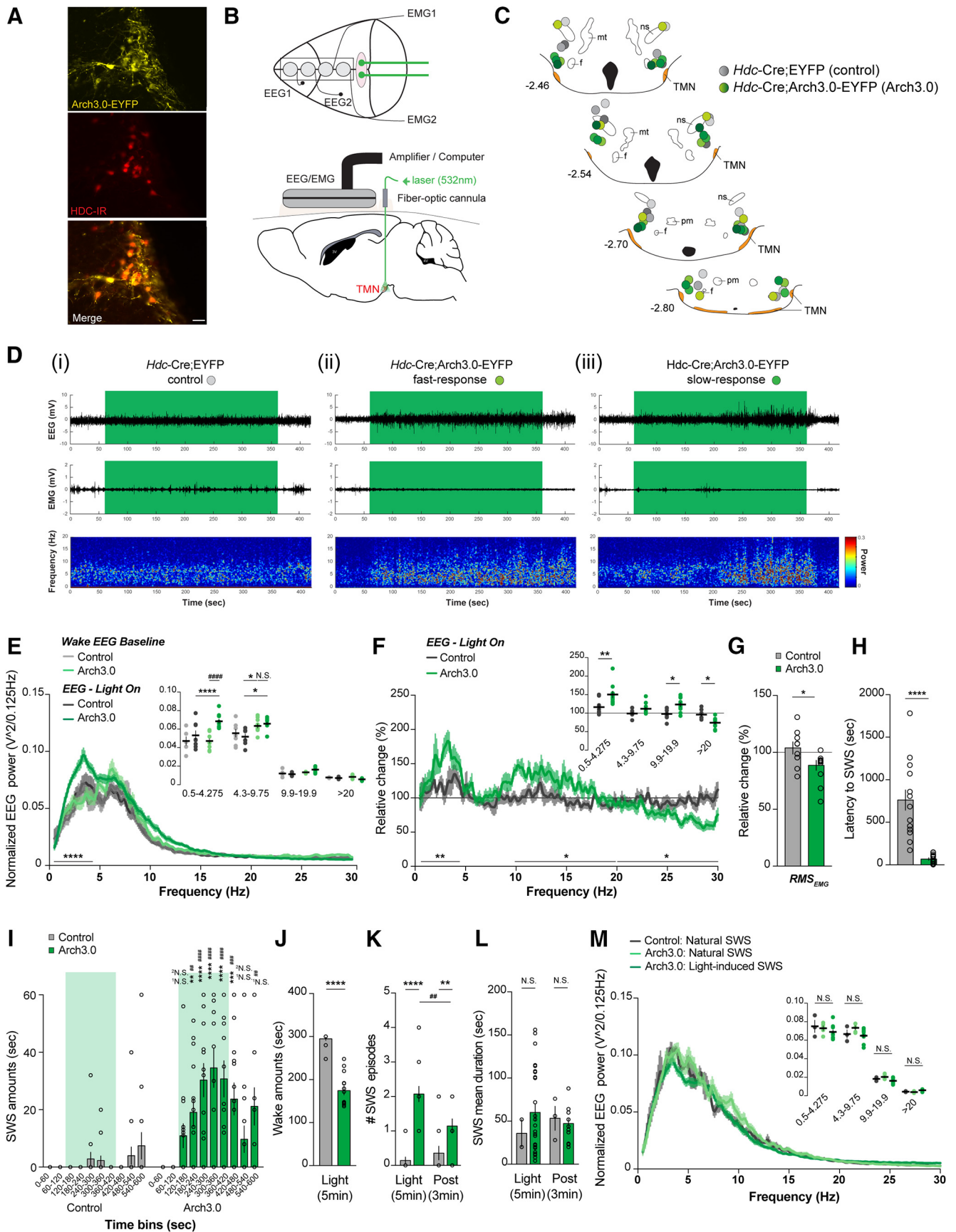

Figure 5. Optogenetic silencing of TMNv HA neurons *in vitro*. **A**, Voltage-clamp responses of a representative Arch3.0-expressing HA neuron in a brain slice to varying intensities of green light (25%, 50%, 75%, 100%) for 1 s ($V_m = -70$ mV). **B**, Silencing of spontaneous activity with green light for 1 s in cell-attached (top) and whole-cell current-clamp configuration (bottom). **C**, Raster plot of repeated optogenetic silencing (top) and the corresponding histogram of the number of action potentials occurring within 50 ms bins (bottom; *n* = 12 cells). **D**, Voltage response of a cell undergoing a hyperpolarizing step of −180 pA, similar in magnitude to photoinhibition. **E**, Silencing of spontaneous activity with green light for 1 min in current-clamp configuration.

ception of a mild increase in EEG power density in the theta band (4.3–9.75 Hz). However, in the following analysis and experiments, we did not observe any light-induced effects in the theta band in either group or during baseline SWS (Fig. 6F,I–K). Taking into account the sample size, it is unclear whether the expression of the Arch3.0-EYFP transgene modifies theta band oscillations while spontaneous EEG SWA and other oscillations, ranging from 9.9 to 30 Hz, are unaffected.

During photoillumination, *Hdc*-Cre;Ach3.0-EYFP mice displayed significant changes in EEG spectral profile with increased SWA, evidenced by high power density in the delta band (0.5–4.25 Hz), compared with what was observed in time-of-day equivalent activity in control mice also receiving photoillumination (0.5–4.25 Hz, *p* < 0.0001; 4.3–9.75 Hz, *p* = 0.77; 9.9–19.9 Hz, *p* = 0.60; >20 Hz, *p* = 0.75). This increase in delta power was highlighted by examining EEG changes in the percentage of baseline (prelight) values (Fig. 6F; 0.5–4.25 Hz, *p* < 0.001). In addition, we observed a significant increase in EEG power density at alpha/gamma/low-beta bands (9.9–19.9 Hz, *p* < 0.05) and a decrease in EEG power density at high frequencies >20 Hz (*p* < 0.05), corresponding to high-beta and low-gamma oscillations,

Figure 6. Optogenetic silencing of TMNv HA neurons in awake and behaving mice induces SWS during the dark, active phase. **A**, Photomicrographs showing the selective targeting of Arch3.0-EYFP expression in HDC-IR neurons. Scale bar, 50 μm. **B**, Schematic of the *in vivo* polysomnography EEG/EMG recording device and optical fiber implantation for bilateral photoillumination of the TMNv. **C**, Schematic of coronal sections showing the location of bilateral optical fiber tips for each animal, which are color coded to reflect genotypes (*Figure legend continues.*)
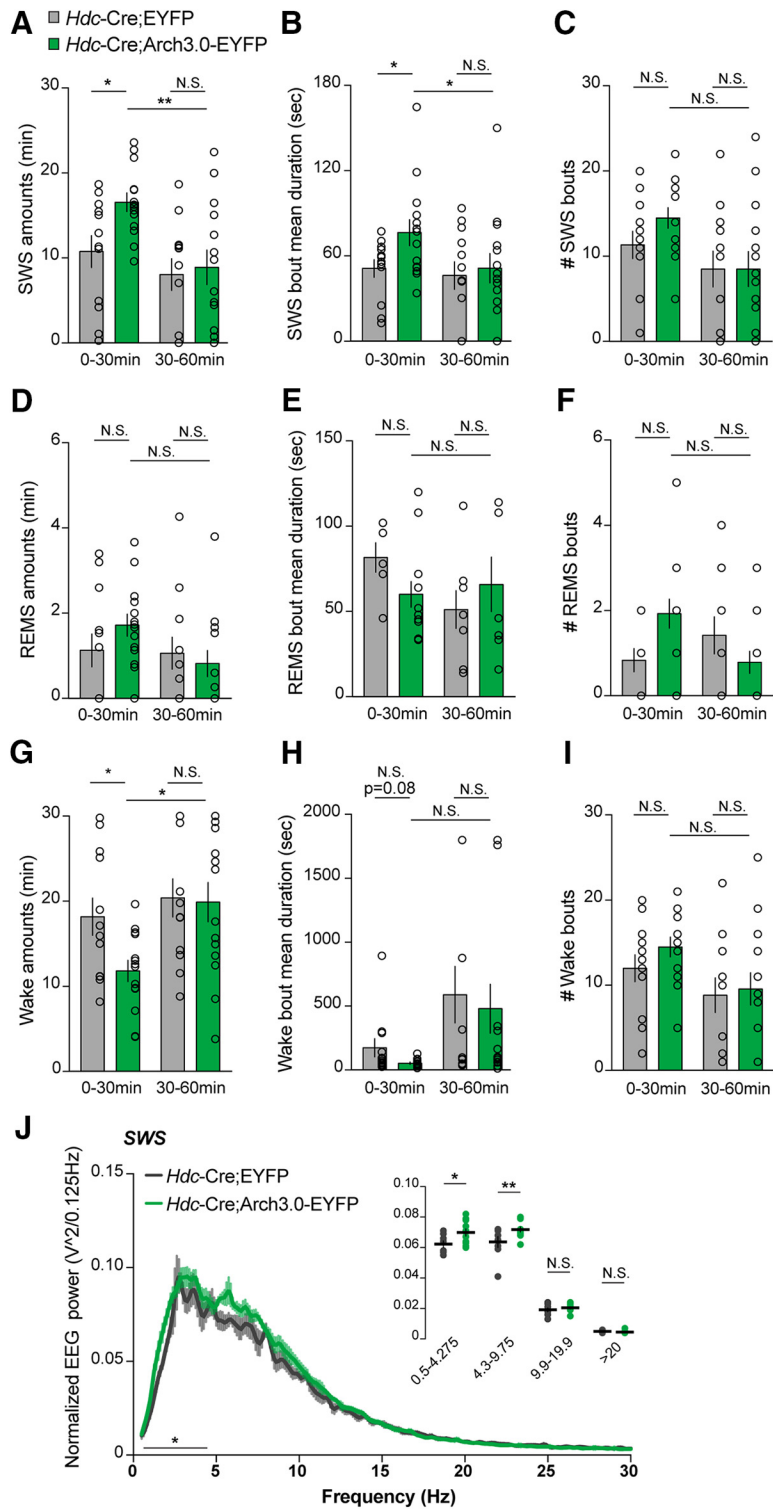
←

(*Figure legend continued.*) *Hdc*-Cre;Arch3.0-EYFP (shades of green) and *Hdc*-Cre;EYFP controls (shades of gray) across the TMN rostrocaudal axis. **D**, Representative EEG/EMG traces and the corresponding heat map of EEG power spectrum illustrating behavioral responses to optogenetic inhibition in control *Hdc*-Cre;EYFP mice (**Di**) and *Hdc*-Cre;Arch3.0-EYFP mice (**Dii, Diii**) during 7 min recordings (7:00 to 10:00 P.M., lights off at 8:00 P.M.). Note the variety of short (**Dii**) and longer (**Diii**) latency responses to 5 min of continuous 532 nm bilateral photoillumination of TMNv HA neurons (green block), marked by the appearance of large slow-wave oscillations, low EMG tone, and increased EEG power. **E**, Cortical EEG power spectra of control *Hdc*-Cre;EYFP and *Hdc*-Cre; Arch3.0-EYFP mice during baseline recording before lights on, when mice are awake (light traces), and during photoillumination (dark traces; $n = 3$ *Hdc*-Cre;EYFP controls, 14 sessions, gray traces; $n = 5$ *Hdc*-Cre;Arch3.0-EYFP mice, 14 sessions, green traces). On the top right corner, graphs represent the mean power densities ($\pm$SEM) in the different frequency bands examined: delta (0.4–4.3 Hz), theta (4.3–9.8 Hz), alpha/gamma/low-beta (9.8–19.9 Hz), and high-beta/low-gamma ($>$20 Hz: 20–30 Hz). Note the significant increase in delta power compared with controls and baseline values in response to light in *Hdc*-Cre;Arch3.0-EYFP mice. **F**, Relative EEG power spectra changes ($\pm$SEM) over baseline (prelight) during the 5 min photoillumination. Top right corner indicates the quantitative changes in the EEG during photoillumination over baseline for the different frequency bands. Note the increase in delta and alpha/gamma/low-beta frequencies and decrease in high-beta/low-gamma frequencies in *Hdc*-Cre;Arch3.0-EYFP mice (green) compared with *Hdc*-Cre;EYFP controls (gray) in response to light. **G**, Relative change in EMG activity. The RMS$_{EMG}$ value during photoillumination was normalized to the corresponding values at prelight baseline stage (Mann–Whitney test, *$p < 0.05$). **H**, Latency to the appearance of SWS from the start of the photoillumination ($n = 3$ *Hdc*-Cre;EYFP controls, 14 sessions; $n = 5$ *Hdc*-Cre;Arch3.0-EYFP, 14 sessions; Mann–Whitney test, ****$p < 0.0001$). **I**, SWS quantities in 1 min time bins starting 2 min before photoillumination, during the 5 min of continuous photoillumination (green block), and 3 min after the termination of photoillumination in both *Hdc*-Cre;EYFP controls (gray) and *Hdc*-Cre;Arch3.0-EYFP mice (green). **J**, Wake quantities during the 5 min photoinhibition period. **K, L**, SWS parameters during the 5 min photoillumination (Light) and during the 3 min after (Post) in both *Hdc*-Cre;EYFP controls (gray) and *Hdc*-Cre;Arch3.0-EYFP mice (green) showing an increase in the number of SWS episodes (**K**) while SWS mean duration remains similar (**L**). **M**, Comparison of EEG power spectra during natural SWS (no-light) of both *Hdc*-Cre;EYFP controls (gray) and *Hdc*-Cre;Arch3.0-EYFP mice (light green), with light-induced SWS in *Hdc*-Cre; Arch3.0-EYFP mice (dark green). Top right corner indicates similar mean values of cortical EEG power densities in the different frequency bands in natural SWS states of both groups and light-induced sleep in *Hdc*-Cre;Arch3.0-EYFP mice. Data are presented as the mean $\pm$ SEM two-way repeated-measures ANOVA to test the interaction among frequency bands, genotype, and stimulation, or between time bins and genotype were first performed followed by *post hoc* Sidak's or Tukey's multiple-comparisons test, Mann–Whitney or Welch's tests represented on the graphs as follows: ****$p < 0.0001$, ***$p < 0.001$, **$p < 0.01$, *$p < 0.05$, [1]N.S. is not significant to compare genotype groups; ####$p < 0.0001$, ###$p < 0.001$, ##$p < 0.01$, #$p < 0.05$, [2]N.S. is not significant to compare frequency bands or time-bins within *Hdc*-Cre;Arch3.0-EYFP mice. EEG power densities during baseline and lights on: interaction between frequency bands and genotype/stimulation, $F_{(9,96)} = 7.1, p < 0.0001$; genotype/stimulation factor, $F_{(3,96)} = 659.9, p < 0.0001$; frequency bands, $F_{(3,32)} = 8.1, p = 0.0004$. Relative EEG power change (%): interaction between frequency bands and genotype, $F_{(3,48)} = 7.5, p = 0.0003$; genotype factor, $F_{(3,48)} = 19.8, p < 0.0001$; frequency bands, $F_{(1,16)} = 13.3, p = 0.002$. SWS amounts: interaction between time bins and genotype, $F_{(9,234)} = 5.3, p < 0.0001$; genotype factor, $F_{(9,234)} = 6.4, p < 0.0001$; time bins, $F_{(1,26)} = 56.6, p < 0.0001$. Number of SWS episodes: interaction between time and genotype, $F_{(1,26)} = 7.3, p = 0.01$; time factor, $F_{(1,26)} = 3.0, p = 0.09$; genotype, $F_{(1,26)} = 67.5, p < 0.0001$. SWS mean duration: interaction between time and genotype, $F_{(1,44)} = 0.6, p = 0.44$; time factor, $F_{(1,44)} = 0.01$, $p = 0.9$; genotype, $F_{(1,44)} = 0.22, p = 0.64$. EEG power densities during baseline SWS and light-induced sleep: interaction between frequency bands and genotype/stimulation, $F_{(6,48)} = 1.6, p = 0.18$; genotype/stimulation factor, $F_{(2,16)} = 3.5, p = 0.06$; frequency bands, $F_{(3,48)} = 647.4, p < 0.0001$.

---

of photoinhibited *Hdc*-Cre;Arch3.0-EYFP mice compared with controls. Given that SWA is a marker of SWS quality and intensity, that increases in gamma power may be indicative of increased sleep spindle activity, and that high EEG frequencies such as beta and gamma bands are indicative of cortical activation and high levels of arousal, our findings suggest that acute inhibition of HA neurons can alter vigilance by promoting SWS and can also influence qualitative aspects of SWS. The induction of SWS is also supported by a decrease in EMG activity in response to light (Fig. 6*D*,*G*). The RMS$_{EMG}$ was examined to process EMG amplitude in response to neuronal photoinhibition (Fig. 6*G*). The mean of the RMS$_{EMG}$ in *Hdc*-Cre;Arch3.0-EYFP mice was found to be significantly lower than that in control *Hdc*-Cre;EYFP mice (Mann–Whitney test, $p = 0.04$), suggesting a reduction of the amplitude of muscle activation. Altogether, these data indicate that the behavioral changes we observe can be defined as SWS or light-induced sleep, terms we will use from here on.

To further characterize and quantify this light-induced sleep state, we examined the latencies to fall asleep and the amounts of SWS during the photoillumination period. Beforehand, we verified that *Hdc*-Cre;Arch3.0-EYFP and control *Hdc*-Cre;EYFP mice display similar amounts of SWS, wake, and REMS during a 12 h baseline recording acquired from 6:00 P.M. to 6:00 A.M. (*Hdc*-Cre;EYFP: SWS, 4.2 $\pm$ 0.03 h; wake, 7.4 $\pm$ 0.02 h; REMS, 0.4 $\pm$ 0.04 h; *Hdc*-Cre;Arch3.0-EYFP: SWS, 4.4 $\pm$ 0.39 h, $p >$ 0.99; wake, 7.3 $\pm$ 0.43 h, $p = 0.79$; REMS, 0.4 $\pm$ 0.05 h, $p > 0.99$). During the photoillumination period, *Hdc*-Cre;Arch3.0-EYFP mice display a significantly shorter latency to fall asleep (67.71 $\pm$ 14.19 s. from lights on, $p < 0.0001$) compared with controls, which rarely show any signs of sleep with a median latency of 12.4 min (761.5 $\pm$ 119 s from lights on; Fig. 6*H*). However, we could distinguish some variability in the response to photoillumination in the form of fast and slow responses among optogenetic sessions in *Hdc*-Cre;Arch3.0-EYFP mice (Fig. 6*Di–Diii*). Independent of the mouse or optical fiber placement, *Hdc*-Cre;Arch3.0-EYFP mice

exhibit SWS either with a short latency (range, 3–60 s) or with a longer latency (after 100–150 s). One explanation may be variation in the number of photoinhibited HA neurons as a result of slight fluctuations in laser output and/or dust in the connectors, which can affect light diffusion and the efficiency of optogenetic inhibition.

Nevertheless, all *Hdc*-Cre;Arch3.0-EYFP mice, across all photoillumination sessions, displayed increasing amounts of SWS once the laser light was delivered compared with the time-of-day sleep–wake cycle of control animals that, in contrast, remained awake, with the exception of two short sleep events in 2 of 14 sessions (Fig. 6*I*; $p < 0.0001$). Accordingly, wake amounts in *Hdc*-Cre;Arch3.0-EYFP (174.4 $\pm$ 9.9 s) are significantly reduced compared with control mice (294.9 $\pm$ 3.9 s) during the 5 min photoinhibition ($p < 0.0001$; Fig. 6*J*). After the termination of photoillumination, effects on SWS (Fig. 6*I*) and wake amounts (data not shown) in *Hdc*-Cre;Arch3.0-EYFP mice last for the subsequent 1 min (both SWS and wake, $p < 0.001$) and return to levels similar to those of controls in the following minute (SWS, $p = 0.97$; Fig. 6*I*; wake, $p = 0.99$; data not shown). The increase in amounts of SWS in *Hdc*-Cre;Arch3.0-EYFP mice mainly results from the occurrence of SWS episodes within the photoinhibition window (Fig. 6*K*,*L*). Indeed, *Hdc*-Cre;Arch3.0-EYFP mice exhibit an average of 2.1 $\pm$ 0.2 episodes of SWS per photoinhibition session ($n = 29$ total $>$14 sessions; Fig. 6*K*), while only two *Hdc*-Cre;EYFP control mice exhibited only one episode of SWS in 1 of 14 sessions, which corresponds to a probability of 14.3% for a sleep event in controls to occur under light exposure ($p < 0.0001$; Fig. 6*K*). This effect is maintained after the termination of photoillumination ($p < 0.01$; Fig. 6*K*) when analyzed over 3 min. Minute-bin analysis in the postphotoinhibition period reflects the changes presented on SWS amounts (Fig. 6*I*), which show significant differences between groups during the first minute following photoinhibition, with an increased number of SWS episodes in *Hdc*-Cre;Arch3.0-EYFP mice (SWS probability of

64.3 ± 13% vs 0% in controls, $p < 0.0001$; data not shown) that return to values similar to those of control mice for the next 2 min (Arch3.0: SWS probability 50 ± 14% vs control SWS probability 21.4 ± 11%, $p = 0.13$; data not shown). These light-induced SWS episodes evoked in *Hdc*-Cre;Arch3.0-EYFP mice have a mean duration of 60.1 ± 9.3 s (Fig. 6*L*), which does not differ from SWS episodes occurring in the control mice during photoinhibition (36 ± 16 s., $p = 0.84$) or after (SWS mean duration: Arch3.0, 47.3 ± 5.6 s; control, 53.3 ± 13.9 s; $p = 0.99$; Fig. 6*L*). However, statistical significance here is weak due to the small number of SWS episodes in controls, notably during the photoinhibition period. These results indicate that light-induced SWS duration is not locked to continuous light exposure and that sleep-to-wake transitions still occur while SWS insertions reappear during the photoillumination period and continue for 1 min after.

To verify that light-induced SWS reflects physiological SWS, we compared spontaneous SWS (no-light) in both conditions (*Hdc*-Cre;EYFP and *Hdc*-Cre; Arch3.0-EYFP), recorded at the equivalent circadian time, with the light-induced SWS power spectrum (Fig. 6*M*). First, we confirmed that both groups exhibit similar spontaneous SWS EEG power spectral profiles and identical power densities in the different frequency bands examined from 0.5 to 30 Hz. Second, we found that light-induced SWS evoked in *Hdc*-Cre; Arch3.0-EYFP mice share the same EEG power spectral profile as natural SWS of

Figure 7. Optogenetic silencing of HA neurons has long-lasting effects on SWS following the termination of photoillumination. Quantitative changes in sleep–wake parameters for 1 h recording after the termination of the photoillumination sessions in *Hdc*-Cre;EYFP controls ($n = 3$ of 14 sessions, gray) and *Hdc*-Cre;Arch3.0-EYFP mice ($n = 5$ of 14 sessions, green). Analysis was divided into two intervals of 30 min: 0 –30 and 30 – 60 min. *A–C*, In the first postphotoillumination interval, previously inhibited *Hdc*-Cre;Arch3.0-EYFP mice exhibit increased amounts of SWS (*A*) resulting from prolonged SWS episode mean duration (*B*), without any change in the number of SWS bouts (*C*). *D–F*, REMS parameters: amounts (in min; D), bout mean duration (*E*), and number of bouts (*F*) are identical between *Hdc*-Cre::Arch-EYFP mice and controls in both postoptogenetic periods. *G–I*, Decrease in wake amounts (*G*) partly result from shorter wake episode mean duration, though the difference is not significant (*H*), and no significant change the number of wake bouts (*I*). In the second postphotoillumination interval (30 – 60 min), SWS parameters and wake amounts return to control values. *J*, Distribution profiles of SWS cortical EEG power spectra from *Hdc*-Cre;EYFP controls ($n = 3$ of 14 sessions, gray) and *Hdc*-Cre;Arch3.0-EYFP mice ($n = 5$ of 14 sessions, green) in the first 30 min postphotoillumination

←

both *Hdc*-Cre;Arch3.0-EYFP mice and controls. Mean EEG power densities, notably in the delta or alpha/gamma and beta/low-gamma frequencies in sleeping *Hdc*-Cre;Arch3.0-EYFP mice, are similar to SWS EEG values during baseline recording with no light in both *Hdc*-Cre;Arch3.0-EYFP and control mice, which suggest that photoinhibition of HA neurons evokes a sleep-like state that resembles physiological SWS (Fig. 6*M*).

Longer-term effects of optogenetic silencing of HA neurons in behaving mice

Finally, to control for the behavioral consequences and reversibility of acute optogenetic photoinhibition of HA neurons, we monitored the sleep–wake cycle of the mice for 1 h following the termination of the light pulse (Fig. 7). Over the subsequent 30 min, *Hdc*-Cre;Arch3.0-EYFP mice exhibit increased amounts of SWS (0–30 min: +15%; $p < 0.05$; Fig. 7*A*), resulting from an elongation in the mean duration of SWS bouts ($p < 0.05$) without affecting the number of SWS episodes ($p = 0.38$; Fig. 7*B*,*C*). In contrast, REMS parameters remain unchanged (Fig. 7*D–F*). The changes we observed in SWS amounts occur at the expense of wakefulness (0–30 min: −16%; $p < 0.05$; Fig. 7*G*), the decrease of which is partly due to shorter wake bout mean duration as the differences between genotypes are not significant with regard to this parameter ($p = 0.08$; Fig. 7*H*). However, the number of wake bouts ($p = 0.4$; Fig. 7*I*) or SWS-to-wake transitions ($p = 0.4$, data not shown) are unchanged. These data suggest possible difficulties in remaining awake over long periods following the termination of HA neuron photoinhibition.

In the following (30–60 min) postphotoillumination period, SWS parameters and wake amounts return to values identical to those in control mice (SWS amounts, $p = 0.93$; SWS bout mean duration, $p = 0.91$; wake amounts, $p = 0.78$; Fig. 7*A*,*B*,*G*). These results indicate that acute photoinhibition of HA neurons in *Hdc*-Cre;Arch3.0-EYFP mice induces long-lasting effects on SWS that are reversed after 30 min and do not result in rebound effects in the subsequent 30 min period. Moreover, we compared SWS EEG power spectral distributions in both *Hdc*-Cre;Arch3.0-EYFP and control *Hdc*-Cre;EYFP mice during the first (0–30 min) interval following photoinhibition and found changes in SWS EEG power spectra with increased SWA in *Hdc*-Cre;Arch3.0-EYFP mice ($p < 0.05$) and higher theta power ($p < 0.01$) compared with SWS EEG profile in control *Hdc*-Cre;EYFP mice (Fig. 7*J*). Importantly, this enhancement of SWA in *Hdc*-Cre;Arch3.0-EYFP in the postinhibition period occurs during the active circadian phase of nocturnal mice, where low levels of SWA are typically observed. However, as discussed earlier, changes in the theta band may not be considered to be specific to the effects of photoillumination. Altogether, these data suggest that acute silencing of HA neuron activity not only participates in the induction and maintenance of sleep but also in the quality and depth of SWS regardless of circadian drive.

Discussion

Using a previously uncharacterized *Hdc*-Cre transgenic line, we performed an anatomical, electrophysiological, and sleep behavioral analysis of genetically identified HA neurons in mice. We found that cre-mediated recombination occurs in TMNv HA neurons with high specificity and minimal extra-TMN expression, though with low/moderate penetrance. In brain slices from *Hdc*-Cre;tdTom mice, we performed a comprehensive analysis of the membrane properties of TMNv HA$^+$ and HA$^-$ neurons. Through hierarchical cluster analysis, we found that HA neurons exhibit unique electrical signatures, and phenotypic diversity

therein, that clearly distinguish them from intermingled neurons in the same region. Finally, we used an optogenetic strategy to acutely silence HA neurons in awake and behaving mice and found that HA neuron photoinhibition induces SWS, but not REMS, followed by a longer-lasting period of SWS enrichment. These results suggest that the silencing of HA neurons during wakefulness not only diminishes arousal but is sufficient to selectively induce SWS.

Although classical experimental work, primarily using sharp microelectrode recording in en bloc or slice preparations from young rats and guinea pigs, have shown that HA neurons exhibit distinctive firing properties, including slow, rhythmic pacemaking, broad APs, and a prominent latency to firing following hyperpolarization (Haas and Reiner, 1988; Weiss et al., 1989; Greene et al., 1990; Kamondi and Reiner, 1991; Schönrock et al., 1991; Llinás and Alonso, 1992; Stevens and Haas, 1996), their functional diversity is unknown. Our hierarchical cluster analysis of TMNv HA$^+$ and HA$^-$ neurons revealed that HA$^+$ neurons exhibit many of these key electrical signatures, which are distinct from HA$^-$ neurons in the same region. We also demonstrated an unexpected functional dichotomy among HA$^+$ neurons (HA$^+$ Types 1 and 2). These data suggest that diversity, or a continuum of functional properties, exists among HA$^+$ neurons even within the compact TMNv. This notion is broadly consistent with evidence that HA neurons may be functionally heterogeneous (Haxhiu et al., 2001; Sergeeva et al., 2001, 2002, 2005; Miklós and Kovács, 2003; Giannoni et al., 2009; Blandina et al., 2012), suggesting that HA neurons are likely organized into distinct circuits that may engage specific physiological outputs (Haas et al., 2008; Giannoni et al., 2009; Blandina et al., 2012). Further work will be required to determine how electrophysiological diversity may align with neurochemical and circuit-level heterogeneity among TMNv neurons.

Numerous lines of neuroanatomical, electrophysiological, and behavioral evidence from multiple experimental preparations suggest that the HA system has a key role in cortical activation and wakefulness (Lin et al., 1989; Schwartz et al., 1991; Nitz and Siegel, 1996; Lin, 2000; Brown et al., 2001; Nelson et al., 2002; Haas and Panula, 2003; Saper et al., 2005; Passani et al., 2007; Haas et al., 2008; Saper et al., 2010; Thakkar, 2011; Panula and Nuutinen, 2013). Notably, HA neurons display wake-specific firing patterns *in vivo* (Steininger et al., 1999; Vanni-Mercier et al., 2003; Takahashi et al., 2006; Sakai et al., 2010). Surprisingly, however, specific loss-of-function manipulations that disrupt HA-mediated neurotransmission (Parmentier et al., 2002, 2016; Gerashchenko et al., 2004; Huang et al., 2006; Anaclet et al., 2009) display relatively modest effects on sleep–wake patterns. As these results may be explained by developmental compensation by other arousal circuits, more acute manipulations of neuronal excitability are required to directly assess the role of the HA system in arousal. In this regard, recent work showed that chemogenetic activation of mouse HA neurons induced a significant increase in locomotor activity, consistent with enhanced arousal (Yu et al., 2015).

Our *in vivo* optogenetic experiments demonstrate that acute silencing of HA neuron activity rapidly induces a sleep state that resembles natural SWS, with cortical SWA, during a period of low sleep pressure. First, little to no differences in baseline wake or SWS EEG power spectra or amounts were detected between control *Hdc*-Cre;EYFP and *Hdc*-Cre;Arch3.0-EYFP mice, while light-induced SWS appears identical to natural SWS. Second, large-amplitude slow oscillations appeared with increased delta power and gradual loss of muscle tone in conjunction with HA

neuron photoinhibition. Furthermore, light-induced SWS appeared with short latencies, which is consistent with the silencing of HA neurons before the onset of sleep and during sleep (Takahashi et al., 2006). This result is also consistent with the effects of selective H1 receptor (H1R) antagonists, which induce cortical SWA and SWS at the expense of wakefulness (Ikeda-Sagara et al., 2012; Parmentier et al., 2016), and with the phenotypes of H1R$^{-/-}$ and HDC$^{-/-}$ mice showing reduced SWS/wake EEG power ratio and an inability to maintain vigilance, with decreased sleep latency, in response to behavioral challenges (Parmentier et al., 2002; Parmentier et al., 2016). Together, these data suggest that the acute cessation of HA-mediated neurotransmission during periods of low sleep pressure facilitates or permits SWS at the expense of wakefulness.

What are the circuit-level mechanisms underlying sleep induction by HA neuron silencing? One possibility emerges from the Flip-Flop Switch Model, a prominent hypothesis for sleep–wake transitions, which predicts that mutually antagonistic connections between GABAergic/galaninergic, sleep-active preoptic area (POA) neurons, such as the ventrolateral preoptic nucleus (VLPO), and wake–active arousal centers, such as the TMN, determine arousal state transitions (Saper et al., 2001, 2010). Anatomical studies demonstrate that wake-active TMN and sleep-active VLPO neurons are reciprocally connected (Sherin et al., 1998; Steininger et al., 2001; Chou et al., 2002; Gaus et al., 2002; Saito et al., 2013). In the VLPO, bath-applied HA (Liu et al., 2010) or optogenetic stimulation of HA axons (Williams et al., 2014) have been shown to excite a population of inhibitory interneurons, resulting in feedforward inhibition of sleep-promoting VLPO neurons. In light of these mechanisms, one plausible effect of acute silencing of HA neurons may be the rapid disinhibition of sleep-active POA neurons and the induction of SWS, which has been observed following chemogenetic activation of GABAergic POA neurons (Saito et al., 2013). Most recently, Dan and colleagues identified a population of GABAergic/neuropeptidergic POA neurons that specifically project to the TMN through retrograde labeling (Chung et al., 2017). Optogenetic activation of these POA neurons, or their axons in the TMN, resulted in a rapid increase in SWS, delayed enhancement in REMS, and decreased wakefulness (Chung et al., 2017). With the exception of increased REMS, the effect of our direct optogenetic silencing of HA neurons is consistent with these results and suggests one circuit-level mechanism through which HA neurons may be rapidly and tonically silenced by inhibitory synaptic input to induce and stabilize SWS. Furthermore, endogenous mechanisms that may account for the suppression of TMN activity during sleep have been probed by Wisden and colleagues using cell type-specific genetic manipulations of GABAergic input onto HA neurons (Zecharia et al., 2012). More recently, they showed that in HA neurons, made selectively sensitive to the hypnotic GABA$_A$ receptor agonist zolpidem, SWS latency was shortened and total sleep time was lengthened (Uygun et al., 2016). These observations also support a model in which the initiation of natural SWS arises through increased and sustained GABAergic input onto HA neurons.

Other arousal pathways, including wake-on locus ceruleus noradrenergic, dorsal raphe serotonergic, basal forebrain cholinergic, or lateral hypothalamic hypocretin/orexin (Hcrt/Ox) neurons can drive or modulate cortical activation and sleep–wake states in parallel with the HA system (Sakurai, 2007; Brown et al., 2012; Weber and Dan, 2016; Jones, 2017; Scammell et al., 2017). Recent cell type-specific optogenetic and chemogenetic manipulation of some of these cell populations and/or their projections

have revealed both unique and overlapping roles in modulating sleep–wake transitions (de Lecea, 2015; Weber and Dan, 2016; Jones, 2017; Scammell et al., 2017). Indeed, this distributed arousal-promoting network shares reciprocal connectivity with the HA system (Haas and Panula, 2003). In particular, its function is interwoven with that of the Hcrt/Ox system (Shan et al., 2015b) whereby Hcrt/Ox neurons constitute a major source of excitatory input onto HA neurons (Bayer et al., 2001; Eriksson et al., 2001; Schöne et al., 2012, 2014) and their effects on arousal stability appear to depend on HA neurons as downstream effectors (Huang et al., 2001), in a manner similar to that in locus ceruleus noradrenergic neurons (Carter et al., 2012). Another reflection of the strong, functional interdependence between HA and Hcrt/Ox neurons is the induction of SWS following chemogenetic or optogenetic silencing of Hcrt/Ox neurons (Sasaki et al., 2011; Tsunematsu et al., 2011, 2013).

Together, our results highlight the unique role that the HA system may play in the mechanisms and pathways responsible for sedation and sleep. Further investigation of the interconnections between the HA system and other arousal circuits, including the modulation of thalamic and cortical circuits (Lőrincz and Adamantidis, 2017), will be required to elucidate the mechanisms underlying the rapid induction of SWS by HA neuron silencing. Finally, the HA system has emerged as an attractive therapeutic target for the treatment of neuropsychiatric and neurodegenerative diseases (Panula and Nuutinen, 2013; Baronio et al., 2014; Shan et al., 2015a,b), and furthering our understanding of the role of HA neurotransmission in arousal and cognition may lead to the identification of novel therapeutic targets.

References

Anaclet C, Parmentier R, Ouk K, Guidon G, Buda C, Sastre JP, Akaoka H, Sergeeva OA, Yanagisawa M, Ohtsu H, Franco P, Haas HL, Lin JS (2009) Orexin/hypocretin and histamine: distinct roles in the control of wakefulness using knock-out mouse models. J Neurosci 29:14423–14438. CrossRef Medline

Baronio D, Gonchoroski T, Castro K, Zanatta G, Gottfried C, Riesgo R (2014) Histaminergic system in brain disorders: lessons from the translational approach and future perspectives. Ann Gen Psychiatry 13:34. CrossRef Medline

Bayer L, Eggermann E, Serafin M, Saint-Mleux B, Machard D, Jones B, Mühlethaler M (2001) Orexins (hypocretins) directly excite tuberomammillary neurons. Eur J Neurosci 14:1571–1575. CrossRef Medline

Bayliss DA, Wang YM, Zahnow CA, Joseph DR, Millhorn DE (1990) Localization of histidine decarboxylase mRNA in rat brain. Mol Cell Neurosci 1:3–9. CrossRef Medline

Blandina P, Munari L, Provensi G, Passani MB (2012) Histamine neurons in the tuberomamillary nucleus: a whole center or distinct subpopulations? Front Syst Neurosci 6:33. CrossRef Medline

Brown RE, Stevens DR, Haas HL (2001) The physiology of brain histamine. Prog Neurobiol 63:637–672. CrossRef Medline

Brown RE, Basheer R, McKenna JT, Strecker RE, McCarley RW (2012) Control of sleep and wakefulness. Physiol Rev 92:1087–1187. CrossRef Medline

Carter ME, Brill J, Bonnavion P, Huguenard JR, Huerta R, de Lecea L (2012) Mechanism for hypocretin-mediated sleep-to-wake transitions. Proc Natl Acad Sci U S A 109:E2635–E2644. CrossRef Medline

Castrén E, Panula P (1990) The distribution of histidine decarboxylase mRNA in the rat brain: an in situ hybridization study using synthetic oligonucleotide probes. Neurosci Lett 120:113–116. CrossRef Medline

Chou TC, Bjorkum AA, Gaus SE, Lu J, Scammell TE, Saper CB (2002) Afferents to the ventrolateral preoptic nucleus. J Neurosci 22:977–990. Medline

Chu M, Huang ZL, Qu WM, Eguchi N, Yao MH, Urade Y (2004) Extracellular histamine level in the frontal cortex is positively correlated with the amount of wakefulness in rats. Neurosci Res 49:417–420. CrossRef Medline

Chung S, Weber F, Zhong P, Tan CL, Nguyen TN, Beier KT, Hörmann N, Chang WC, Zhang Z, Do JP, Yao S, Krashes MJ, Tasic B, Cetin A, Zeng H, Knight ZA, Luo L, Dan Y (2017) Identification of preoptic sleep neurons using retrograde labelling and gene profiling. Nature 545:477–481. CrossRef Medline

de Lecea L (2015) Optogenetic control of hypocretin (orexin) neurons and arousal circuits. Curr Top Behav Neurosci 25:367–378. CrossRef Medline

Ericson H, Watanabe T, Köhler C (1987) Morphological analysis of the tuberomammillary nucleus in the rat brain: delineation of subgroups with antibody against L-histidine decarboxylase as a marker. J Comp Neurol 263:1–24. CrossRef Medline

Eriksson KS, Sergeeva O, Brown RE, Haas HL (2001) Orexin/hypocretin excites the histaminergic neurons of the tuberomammillary nucleus. J Neurosci 21:9273–9279. Medline

Gaus SE, Strecker RE, Tate BA, Parker RA, Saper CB (2002) Ventrolateral preoptic nucleus contains sleep-active, galaninergic neurons in multiple mammalian species. Neuroscience 115:285–294. CrossRef Medline

Gerashchenko D, Chou TC, Blanco-Centurion CA, Saper CB, Shiromani PJ (2004) Effects of lesions of the histaminergic tuberomammillary nucleus on spontaneous sleep in rats. Sleep 27:1275–1281. CrossRef Medline

Giannoni P, Passani MB, Nosi D, Chazot PL, Shenton FC, Medhurst AD, Munari L, Blandina P (2009) Heterogeneity of histaminergic neurons in the tuberomammillary nucleus of the rat. Eur J Neurosci 29:2363–2374. CrossRef Medline

Gong S, Zheng C, Doughty ML, Losos K, Didkovsky N, Schambra UB, Nowak NJ, Joyner A, Leblanc G, Hatten ME, Heintz N (2003) A gene expression atlas of the central nervous system based on bacterial artificial chromosomes. Nature 425:917–925. CrossRef Medline

Gong S, Doughty M, Harbaugh CR, Cummins A, Hatten ME, Heintz N, Gerfen CR (2007) Targeting Cre recombinase to specific neuron populations with bacterial artificial chromosome constructs. J Neurosci 27:9817–9823. CrossRef Medline

Greene RW, Haas HL, Reiner PB (1990) Two transient outward currents in histamine neurons of the rat hypothalamus in vitro. J Physiol 420:149–163. CrossRef Medline

Haas H, Panula P (2003) The role of histamine and the tuberomamillary nucleus in the nervous system. Nat Rev Neurosci 4:121–130. CrossRef Medline

Haas HL, Reiner PB (1988) Membrane properties of histaminergic tuberomammillary neurons of the rat hypothalamus in vitro. J Physiol 399:633–646. CrossRef Medline

Haas HL, Sergeeva OA, Selbach O (2008) Histamine in the nervous system. Physiol Rev 88:1183–1241. CrossRef Medline

Harris JA, Hirokawa KE, Sorensen SA, Gu H, Mills M, Ng LL, Bohn P, Mortrud M, Ouellette B, Kidney J, Smith KA, Dang C, Sunkin S, Bernard A, Oh SW, Madisen L, Zeng H (2014) Anatomical characterization of Cre driver mice for neural circuit mapping and manipulation. Front Neural Circuits 8:76. CrossRef Medline

Haxhiu MA, Tolentino-Silva F, Pete G, Kc P, Mack SO (2001) Monoaminergic neurons, chemosensation and arousal. Respir Physiol 129:191–209. CrossRef Medline

Hayashi H, Takagi H, Takeda N, Kubota Y, Tohyama M, Watanabe T, Wada H (1984) Fine structure of histaminergic neurons in the caudal magnocellular nucleus of the rat as demonstrated by immunocytochemistry using histidine decarboxylase as a marker. J Comp Neurol 229:233–241. CrossRef Medline

Huang ZL, Qu WM, Li WD, Mochizuki T, Eguchi N, Watanabe T, Urade Y, Hayaishi O (2001) Arousal effect of orexin A depends on activation of the histaminergic system. Proc Natl Acad Sci U S A 98:9965–9970. CrossRef Medline

Huang ZL, Mochizuki T, Qu WM, Hong ZY, Watanabe T, Urade Y, Hayaishi O (2006) Altered sleep-wake characteristics and lack of arousal response to H3 receptor antagonist in histamine H1 receptor knockout mice. Proc Natl Acad Sci U S A 103:4687–4692. CrossRef Medline

Ikeda-Sagara M, Ozaki T, Shahid M, Morioka E, Wada K, Honda K, Hori A, Matsuya Y, Toyooka N, Ikeda M (2012) Induction of prolonged, continuous slow-wave sleep by blocking cerebral H1 histamine receptors in rats. Br J Pharmacol 165:167–182. CrossRef Medline

Inagaki N, Yamatodani A, Ando-Yamamoto M, Tohyama M, Watanabe T, Wada H (1988) Organization of histaminergic fibers in the rat brain. J Comp Neurol 273:283–300. CrossRef Medline

Jackson AC, Bean BP (2007) State-dependent enhancement of subthreshold

A-type potassium current by 4-aminopyridine in tuberomammillary nucleus neurons. J Neurosci 27:10785–10796. CrossRef Medline

Jones BE (2017) Principal cell types of sleep-wake regulatory circuits. Curr Opin Neurobiol 44:101–109. CrossRef Medline

Kamondi A, Reiner PB (1991) Hyperpolarization-activated inward current in histaminergic tuberomammillary neurons of the rat hypothalamus. J Neurophysiol 66:1902–1911. Medline

Karlstedt K, Nissinen M, Michelsen KA, Panula P (2001) Multiple sites of L-histidine decarboxylase expression in mouse suggest novel developmental functions for histamine. Dev Dyn 221:81–91. CrossRef Medline

Ko EM, Estabrooke IV, McCarthy M, Scammell TE (2003) Wake-related activity of tuberomammillary neurons in rats. Brain Res 992:220–226. CrossRef Medline

Lin JS (2000) Brain structures and mechanisms involved in the control of cortical activation and wakefulness, with emphasis on the posterior hypothalamus and histaminergic neurons. Sleep Med Rev 4:471–503. CrossRef Medline

Lin JS, Sakai K, Jouvet M (1988) Evidence for histaminergic arousal mechanisms in the hypothalamus of cat. Neuropharmacology 27:111–122. CrossRef Medline

Lin JS, Sakai K, Vanni-Mercier G, Jouvet M (1989) A critical role of the posterior hypothalamus in the mechanisms of wakefulness determined by microinjection of muscimol in freely moving cats. Brain Res 479:225–240. CrossRef Medline

Lin JS, Sakai K, Jouvet M (1994) Hypothalamo-preoptic histaminergic projections in sleep-wake control in the cat. Eur J Neurosci 6:618–625. CrossRef Medline

Lin JS, Sergeeva OA, Haas HL (2011) Histamine H3 receptors and sleep-wake regulation. J Pharmacol Exp Ther 336:17–23. CrossRef Medline

Liu YW, Li J, Ye JH (2010) Histamine regulates activities of neurons in the ventrolateral preoptic nucleus. J Physiol 588:4103–4116. CrossRef Medline

Llinás RR, Alonso A (1992) Electrophysiology of the mammillary complex in vitro. I. Tuberomammillary and lateral mammillary neurons. J Neurophysiol 68:1307–1320. Medline

Lőrincz ML, Adamantidis AR (2017) Monoaminergic control of brain states and sensory processing: existing knowledge and recent insights obtained with optogenetics. Prog Neurobiol 151:237–253. CrossRef Medline

Madisen L, Zwingman TA, Sunkin SM, Oh SW, Zariwala HA, Gu H, Ng LL, Palmiter RD, Hawrylycz MJ, Jones AR, Lein ES, Zeng H (2010) A robust and high-throughput Cre reporting and characterization system for the whole mouse brain. Nat Neurosci 13:133–140. CrossRef Medline

McGinty DJ (1969) Somnolence, recovery and hyposomnia following ventro-medial diencephalic lesions in the rat. Electroencephalogr Clin Neurophysiol 26:70–79. CrossRef Medline

Miklós IH, Kovács KJ (2003) Functional heterogeneity of the responses of histaminergic neuron subpopulations to various stress challenges. Eur J Neurosci 18:3069–3079. CrossRef Medline

Naquet R, Denavit M, Albe-Fessard D (1966) Comparison between the role of the subthalamus and that of the different bulbomesencephalic structures in the maintenance of wakefulness. Electroencephalogr Clin Neurophysiol 20:149–164. CrossRef Medline

Nelson LE, Guo TZ, Lu J, Saper CB, Franks NP, Maze M (2002) The sedative component of anesthesia is mediated by GABA(A) receptors in an endogenous sleep pathway. Nat Neurosci 5:979–984. CrossRef Medline

Nicholson AN, Pascoe PA, Turner C, Ganellin CR, Greengrass PM, Casy AF, Mercer AD (1991) Sedation and histamine H1-receptor antagonism: studies in man with the enantiomers of chlorpheniramine and dimethindene. Br J Pharmacol 104:270–276. CrossRef Medline

Nitz D, Siegel JM (1996) GABA release in posterior hypothalamus across sleep-wake cycle. Am J Physiol 271:R1707–R1712. Medline

Panula P, Nuutinen S (2013) The histaminergic network in the brain: basic organization and role in disease. Nat Rev Neurosci 14:472–487. CrossRef Medline

Panula P, Yang HY, Costa E (1984) Histamine-containing neurons in the rat hypothalamus. Proc Natl Acad Sci U S A 81:2572–2576. CrossRef Medline

Panula P, Pirvola U, Auvinen S, Airaksinen MS (1989) Histamine-immunoreactive nerve fibers in the rat brain. Neuroscience 28:585–610. CrossRef Medline

Parmentier R, Ohtsu H, Djebbara-Hannas Z, Valatx JL, Watanabe T, Lin JS (2002) Anatomical, physiological, and pharmacological characteristics of histidine decarboxylase knock-out mice: evidence for the role of brain

histamine in behavioral and sleep-wake control. J Neurosci 22:7695–7711. Medline

Parmentier R, Zhao Y, Perier M, Akaoka H, Lintunen M, Hou Y, Panula P, Watanabe T, Franco P, Lin JS (2016) Role of histamine H1-receptor on behavioral states and wake maintenance during deficiency of a brain activating system: a study using a knockout mouse model. Neuropharmacology 106:20 –34. CrossRef Medline

Passani MB, Blandina P (2011) Histamine receptors in the CNS as targets for therapeutic intervention. Trends Pharmacol Sci 32:242–249. CrossRef Medline

Passani MB, Giannoni P, Bucherelli C, Baldi E, Blandina P (2007) Histamine in the brain: beyond sleep and memory. Biochem Pharmacol 73:1113–1122. CrossRef Medline

Paxinos G, Franklin K (2012) Paxinos and Franklin's the mouse brain in stereotaxic coordinates, Ed 4. New York: Academic.

Reiner PB, McGeer EG (1987) Electrophysiological properties of cortically projecting histamine neurons of the rat hypothalamus. Neurosci Lett 73:43– 47. CrossRef Medline

Saito YC, Tsujino N, Hasegawa E, Akashi K, Abe M, Mieda M, Sakimura K, Sakurai T (2013) GABAergic neurons in the preoptic area send direct inhibitory projections to orexin neurons. Front Neural Circuits 7:192. CrossRef Medline

Sakai K, Takahashi K, Anaclet C, Lin JS (2010) Sleep-waking discharge of ventral tuberomammillary neurons in wild-type and histidine decarboxylase knock-out mice. Front Behav Neurosci 4:53. CrossRef Medline

Sakurai T (2007) The neural circuit of orexin (hypocretin): maintaining sleep and wakefulness. Nat Rev Neurosci 8:171–181. CrossRef Medline

Saper CB, Chou TC, Scammell TE (2001) The sleep switch: hypothalamic control of sleep and wakefulness. Trends Neurosci 24:726–731. CrossRef Medline

Saper CB, Scammell TE, Lu J (2005) Hypothalamic regulation of sleep and circadian rhythms. Nature 437:1257–1263. CrossRef Medline

Saper CB, Fuller PM, Pedersen NP, Lu J, Scammell TE (2010) Sleep state switching. Neuron 68:1023–1042. CrossRef Medline

Sasaki K, Suzuki M, Mieda M, Tsujino N, Roth B, Sakurai T (2011) Pharmacogenetic modulation of orexin neurons alters sleep/wakefulness states in mice. PLoS One 6:e20360. CrossRef Medline

Scammell TE, Arrigoni E, Lipton JO (2017) Neural circuitry of wakefulness and sleep. Neuron 93:747–765. CrossRef Medline

Schöne C, Cao ZF, Apergis-Schoute J, Adamantidis A, Sakurai T, Burdakov D (2012) Optogenetic probing of fast glutamatergic transmission from hypocretin/orexin to histamine neurons in situ. J Neurosci 32:12437–12443. CrossRef Medline

Schöne C, Apergis-Schoute J, Sakurai T, Adamantidis A, Burdakov D (2014) Coreleased orexin and glutamate evoke nonredundant spike outputs and computations in histamine neurons. Cell Rep 7:697–704. CrossRef Medline

Schönrock B, Büsselberg D, Haas HL (1991) Properties of tuberomammillary histamine neurones and their response to galanin. Agents Actions 33:135–137. CrossRef Medline

Schwartz JC (2011) The histamine H3 receptor: from discovery to clinical trials with pitolisant. Br J Pharmacol 163:713–721. CrossRef Medline

Schwartz JC, Arrang JM, Garbarg M, Pollard H, Ruat M (1991) Histaminergic transmission in the mammalian brain. Physiol Rev 71:1–51. Medline

Sergeeva OA, Eriksson KS, Haas HL (2001) Glycine receptor mediated responses in rat histaminergic neurons. Neurosci Lett 300:5–8. CrossRef Medline

Sergeeva OA, Eriksson KS, Sharonova IN, Vorobjev VS, Haas HL (2002) GABA(A) receptor heterogeneity in histaminergic neurons. Eur J Neurosci 16:1472–1482. CrossRef Medline

Sergeeva OA, Andreeva N, Garret M, Scherer A, Haas HL (2005) Pharmacological properties of GABA_A receptors in rat hypothalamic neurons expressing the epsilon-subunit. J Neurosci 25:88–95. CrossRef Medline

Shan L, Bao AM, Swaab DF (2015a) The human histaminergic system in neuropsychiatric disorders. Trends Neurosci 38:167–177. CrossRef Medline

Shan L, Dauvilliers Y, Siegel JM (2015b) Interactions of the histamine and hypocretin systems in CNS disorders. Nat Rev Neurol 11:401– 413. CrossRef Medline

Sherin JE, Elmquist JK, Torrealba F, Saper CB (1998) Innervation of histaminergic tuberomammillary neurons by GABAergic and galaninergic

neurons in the ventrolateral preoptic nucleus of the rat. J Neurosci 18:4705– 4721. Medline

Steininger TL, Alam MN, Gong H, Szymusiak R, McGinty D (1999) Sleep-waking discharge of neurons in the posterior lateral hypothalamus of the albino rat. Brain Res 840:138–147. CrossRef Medline

Steininger TL, Gong H, McGinty D, Szymusiak R (2001) Subregional organization of preoptic area/anterior hypothalamic projections to arousal-related monoaminergic cell groups. J Comp Neurol 429:638–653. CrossRef Medline

Stevens DR, Haas HL (1996) Calcium-dependent prepotentials contribute to spontaneous activity in rat tuberomammillary neurons. J Physiol 493:747–754. CrossRef Medline

Stevens DR, Eriksson KS, Brown RE, Haas HL (2001) The mechanism of spontaneous firing in histamine neurons. Behav Brain Res 124:105–112. CrossRef Medline

Strecker RE, Nalwalk J, Dauphin LJ, Thakkar MM, Chen Y, Ramesh V, Hough LB, McCarley RW (2002) Extracellular histamine levels in the feline preoptic/anterior hypothalamic area during natural sleep-wakefulness and prolonged wakefulness: an in vivo microdialysis study. Neuroscience 113:663–670. CrossRef Medline

Swett CP, Hobson JA (1968) The effects of posterior hypothalamic lesions on behavioral and electrographic manifestations of sleep and waking in cats. Arch Ital Biol 106:283–293. Medline

Takagi H, Morishima Y, Matsuyama T, Hayashi H, Watanabe T, Wada H (1986) Histaminergic axons in the neostriatum and cerebral cortex of the rat: a correlated light and electron microscopic immunocytochemical study using histidine decarboxylase as a marker. Brain Res 364:114–123. CrossRef Medline

Takahashi K, Lin JS, Sakai K (2006) Neuronal activity of histaminergic tuberomammillary neurons during wake-sleep states in the mouse. J Neurosci 26:10292–10298. CrossRef Medline

Takeda N, Inagaki S, Shiosaka S, Taguchi Y, Oertel WH, Tohyama M, Watanabe T, Wada H (1984) Immunohistochemical evidence for the coexistence of histidine decarboxylase-like and glutamate decarboxylase-like immunoreactivities in nerve cells of the magnocellular nucleus of the posterior hypothalamus of rats. Proc Natl Acad Sci U S A 81:7647–7650. CrossRef Medline

Thakkar MM (2011) Histamine in the regulation of wakefulness. Sleep Med Rev 15:65–74. CrossRef Medline

Tsunematsu T, Kilduff TS, Boyden ES, Takahashi S, Tominaga M, Yamanaka A (2011) Acute optogenetic silencing of orexin/hypocretin neurons induces slow-wave sleep in mice. J Neurosci 31:10529–10539. CrossRef Medline

Tsunematsu T, Tabuchi S, Tanaka KF, Boyden ES, Tominaga M, Yamanaka A (2013) Long- lasting silencing of orexin/hypocretin neurons using archaerhodopsin induces slow-wave sleep in mice. Behav Brain Res 255:64–74. CrossRef Medline

Uygun DS, Ye Z, Zecharia AY, Harding EC, Yu X, Yustos R, Vyssotski AL, Brickley SG, Franks NP, Wisden W (2016) Bottom-up versus top-down induction of sleep by zolpidem acting on histaminergic and neocortex neurons. J Neurosci 36:11171–11184. CrossRef Medline

Vanni-Mercier G, Gigout S, Debilly G, Lin JS (2003) Waking selective neurons in the posterior hypothalamus and their response to histamine H3-receptor ligands: an electrophysiological study in freely moving cats. Behav Brain Res 144:227–241. CrossRef Medline

Walker AK, Park WM, Chuang JC, Perello M, Sakata I, Osborne-Lawrence S, Zigman JM (2013) Characterization of gastric and neuronal histaminergic populations using a transgenic mouse model. PLoS One 8:e60276. CrossRef Medline

Ward JH (1963) Hierarchical grouping to optimize an objective function. J Am Stat Assoc 58:236–244. CrossRef

Watanabe T, Taguchi Y, Hayashi H, Tanaka J, Shiosaka S, Tohyama M, Kubota H, Terano Y, Wada H (1983) Evidence for the presence of a histaminergic neuron system in the rat brain: an immunohistochemical analysis. Neurosci Lett 39:249–254. CrossRef Medline

Watanabe T, Taguchi Y, Shiosaka S, Tanaka J, Kubota H, Terano Y, Tohyama M, Wada H (1984) Distribution of the histaminergic neuron system in the central nervous system of rats; a fluorescent immunohistochemical analysis with histidine decarboxylase as a marker. Brain Res 295:13–25. CrossRef Medline

Weber F, Dan Y (2016) Circuit-based interrogation of sleep control. Nature 538:51–59. CrossRef Medline

Weiss ML, Yang QZ, Hatton GI (1989) Magnocellular tuberomammillary

nucleus input to the supraoptic nucleus in the rat: anatomical and in vitro electrophysiological investigations. Neuroscience 31:299–311. CrossRef Medline

Williams RH, Chee MJ, Kroeger D, Ferrari LL, Maratos-Flier E, Scammell TE, Arrigoni E (2014) Optogenetic-mediated release of histamine reveals distal and autoregulatory mechanisms for controlling arousal. J Neurosci 34:6023–6029. CrossRef Medline

Wouterlood FG, Sauren YM, Steinbusch HW (1986) Histaminergic neurons in the rat brain: correlative immunocytochemistry, Golgi impregnation, and electron microscopy. J Comp Neurol 252:227–244. CrossRef Medline

Yanovsky Y, Zigman JM, Kernder A, Bein A, Sakata I, Osborne-Lawrence S, Haas HL, Sergeeva OA (2012) Proton- and ammonium-sensing by histaminergic neurons controlling wakefulness. Front Syst Neurosci 6:23. CrossRef Medline

Yu X, Zecharia A, Zhang Z, Yang Q, Yustos R, Jager P, Vyssotski AL, May-

wood ES, Chesham JE, Ma Y, Brickley SG, Hastings MH, Franks NP, Wisden W (2014) Circadian factor BMAL1 in histaminergic neurons regulates sleep architecture. Curr Biol 24:2838–2844. CrossRef Medline

Yu X, Ye Z, Houston CM, Zecharia AY, Ma Y, Zhang Z, Uygun DS, Parker S, Vyssotski AL, Yustos R, Franks NP, Brickley SG, Wisden W (2015) Wakefulness is governed by GABA and histamine cotransmission. Neuron 87:164–178. CrossRef Medline

Zant JC, Rozov S, Wigren HK, Panula P, Porkka-Heiskanen T (2012) Histamine release in the basal forebrain mediates cortical activation through cholinergic neurons. J Neurosci 32:13244–13254. CrossRef Medline

Zecharia AY, Yu X, Götz T, Ye Z, Carr DR, Wulff P, Bettler B, Vyssotski AL, Brickley SG, Franks NP, Wisden W (2012) GABAergic inhibition of histaminergic neurons regulates active waking but not the sleep-wake switch or propofol-induced loss of consciousness. J Neurosci 32:13062–13075. CrossRef Medline